Volume 24
DOE/DP40200-04

LLE Review

Quarterly Report

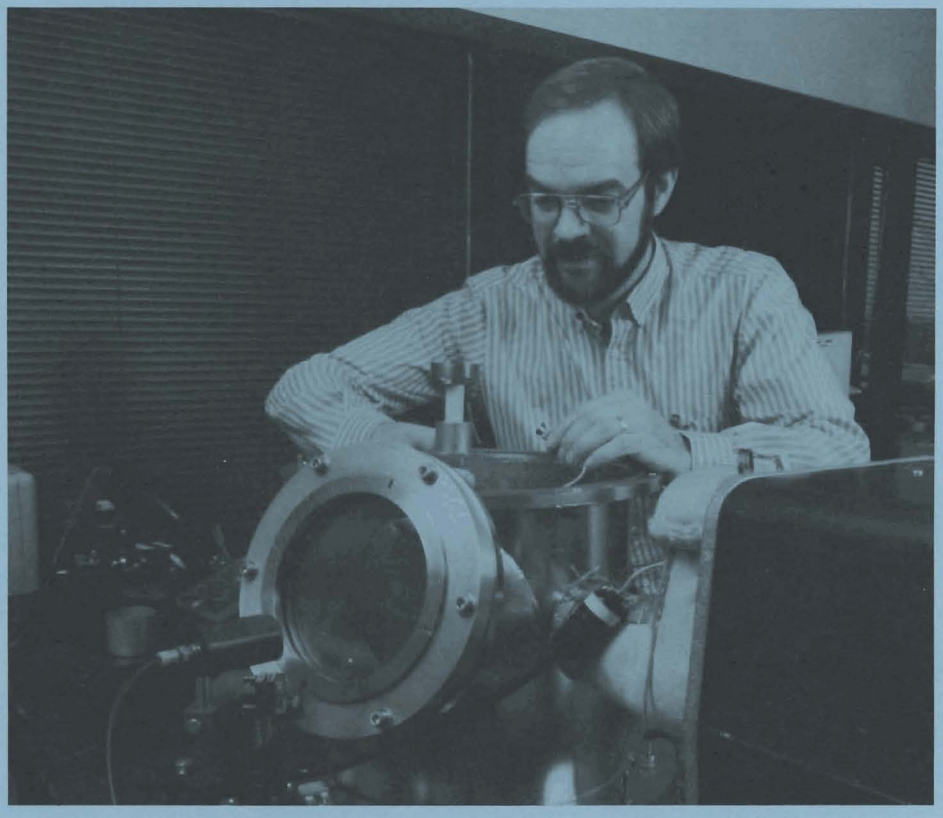

July–September 1985

Laboratory for Laser Energetics
College of Engineering and Applied Science
University of Rochester
250 East River Road
Rochester, New York 14623-1299

Volume 24
DOE/DP40200-04

LLE Review

Quarterly Report

Editor: S. Skupsky
(716) 275-3951

July–September 1985

Laboratory for Laser Energetics
College of Engineering and Applied Science
University of Rochester
250 East River Road
Rochester, New York 14623-1299

This report was prepared as an account of work conducted by the Laboratory for Laser Energetics and sponsored by Empire State Electric Energy Research Corporation, General Electric Company, New York State Energy Research and Development Authority, Northeast Utilities Service Company, Ontario Hydro, Southern California Edison Company, The Standard Oil Company, University of Rochester, the U.S. Department of Energy, and other United States government agencies.

IN BRIEF

This volume of the LLE Review contains articles on the first 24-beam UV experiments on the OMEGA laser system, the use of absorption spectroscopy to diagnose high-density compressions, the development of a new target fabrication technique to coat mechanically unsupported laser-fusion targets with a parylene layer, the use of liquid crystals as laser-beam apodizers, the investigation of the process of melting using a subpicosecond probe, the development of a new picosecond oscilloscope, and the National Laser Users Facility activities for June–September 1985.

The following are some highlights of the work described in this issue:

- The first 24-beam UV implosion experiments on OMEGA are being analyzed using data from a large array of diagnostics, including time-integrated and time-resolved x-ray photography for target imaging, and knock-on fuel-ion spectrometry and neutron activation to measure the individual areal densities ρR of the target fuel and shell.

- The output of the GDL laser system has been increased to 642 J in the IR (1054 nm) and to 236 J at the second harmonic by the addition of active mirror amplifiers.

- Future high-density experiments planned for OMEGA are expected to have compressed, high-opacity shells that would

block x-ray emission from the compressed core of the target. For these targets, absorption spectroscopy might be a suitable diagnostic to examine the compression of signature layers within the target shell. Computer simulations of this process are discussed.

- In the deposition of plastic coatings on fusion targets, the stalk supporting the target can also become coated, resulting in a massive support system that can substantially perturb the implosion. A technique has been developed to perform parylene vapor deposition on levitated targets. A thin stalk can then be attached after the coating is complete.

- Liquid crystal soft apertures have been developed for laser-beam shaping. The liquid crystal compounds used exhibit a high laser-damage resistance and low absorption, making the device applicable to high-peak-power and high-average-power laser systems operating from the UV to IR.

- Picosecond electron diffraction is used to produce an unambiguous picture of the atomic structure of aluminum during laser-induced melting. Breakdown of the lattice structure is observed and interpreted in terms of the defect theory of melting.

- A conceptually new oscilloscope has been developed, capable of subpicosecond resolution. The new electro-electron optic oscilloscope maintains the salient features of the previously used electro-optic technique while eliminating the need for a complex short-pulse laser system.

CONTENTS

Roger Gram, a senior technical associate in the Target Fabrication Group, prepares a chamber for coating targets with plastic ablation layers. The targets are coated while they are being bounced in order to avoid the asymmetry introduced by a supporting stalk.

Section 1
LASER SYSTEM REPORT

1.A GDL Facility Report

The GDL laser system upgrade was completed in July. The new actively mode-locked, Q-switched (AMQ) oscillator, predriver, zoom spatial filters, and active mirror amplifiers were installed, and the system configuration improved. The system became operational in August as an experimental facility and provided target shots for the National Laser Users Facility (UCLA) and LLE experimenters. A highlight of the GDL campaign, during this quarter, has been the excellent performance of the active mirror amplifiers, which have driven the GDL output energy to over 642 J, in the IR (1054 nm) with a 1-ns pulse width, and the achievement of over 236 J at the second harmonic. GDL is scheduled to be converted to the third harmonic during the month of October. A diagram of the upgraded GDL laser appears in Fig. 24.1.

A summary of GDL operations this quarter follows:

System-Pointing, Activation Shots	128
Calorimetry Calibration and Test Shots	101
Target Shots	45
TOTAL	274

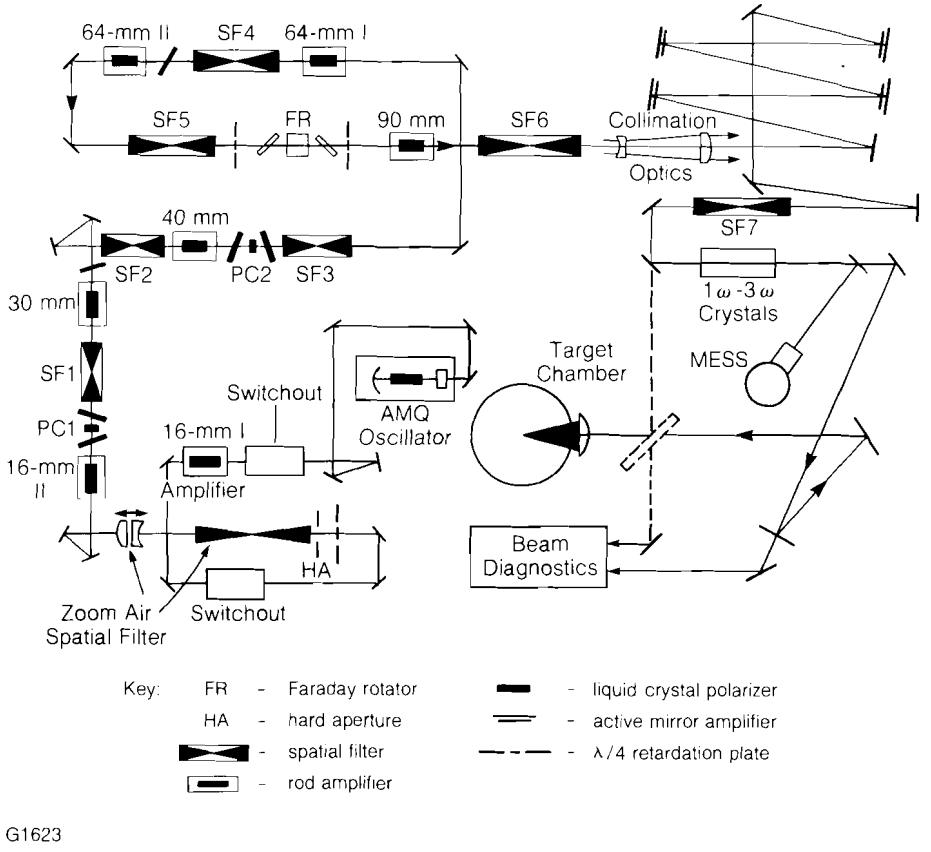

Fig. 24.1
Diagram of the GDL layout.

ACKNOWLEDGMENT

This work was supported by the U.S. Department of Energy Office of Inertial Fusion under agreement number DE-FC08-85DP40200 and by the Laser Fusion Feasibility Project at the Laboratory for Laser Energetics which has the following sponsors: Empire State Electric Energy Research Corporation, General Electric Company, New York State Energy Research and Development Authority, Northeast Utilities Service Company, Ontario Hydro, Southern California Edison Company, The Standard Oil Company, and University of Rochester. Such support does not imply endorsement of the content by any of the above parties.

1.B OMEGA Facility Report

Operations of the OMEGA laser system this quarter consisted of the conclusion of the first 24-beam UV irradiation experiments, and the complete changeover of the oscillator and driver front end of the laser system to a new configuration.

Experiments were conducted in laser-matter interaction, thermal transport, diagnostic development and activation, and implosion studies. Collaborative experiments with the Los Alamos National Laboratory and the Lawrence Livermore National Laboratory involved x-ray conversion

studies and radiation chemistry experiments. Experiments for the National Laser Users Facility were performed by the University of Florida, the University of Maryland, the Naval Research Laboratory, and the Lawrence Berkeley Laboratory. The laser operated routinely at the 2-kJ level, with an energy beam balance of ±5%.

New diagnostic instruments were activated during this period, including several x-ray streak cameras, some with UV (250-nm) time fiducials correlated to laser-on-target time. The fiducial was provided by a small amount of leakage from the final 64-mm amplifier in the driver, which was transported to the target chamber, frequency quadrupled to the fourth harmonic, and coupled via fiber optic to the streak camera's photocathode.

A summary of OMEGA operations this quarter follows:

Driver Test Shots		51
Laser Diagnostic Shots		2
Target Shots		88
	TOTAL	141

Since February, 628 system shots have been taken, corresponding to approximately 25 shots per week. Some highlights of the period include (a) most energy on target: 2.4 kJ with 4.8% beam balance; (b) best beam balance for 24 beams: 3.5% with 2.3 kJ on target; and (c) highest neutron yield: 2×10^{11} with 2.4 kJ on target at 6% beam balance. Operation as a target facility was suspended in late July for front-end conversion.

The conversion consists of installation and activation of a new AMQ oscillator, predriver, and zoom spatial filter into the OMEGA driver. Work is scheduled for completion at the beginning of the first quarter of FY86. The oscillator employs a Nd:YLF rod, which is a departure from the Nd:glass used until now. This oscillator will allow a much higher repetition rate, especially useful for small signal tuning of frequency conversion cells, and for synchronization with a similar oscillator in GDL, which will be critical for 25th-beam x-ray backlighting on OMEGA (scheduled for late fall activation). A new switchout system, employing hard-tube pockels cell drivers (which receive their triggers from within the AMQ electronics) has also been installed. The zoom will allow beam profile control, via various fill factors presented to the amplifiers in the driver line. A diagram of the new driver configuration appears in Fig. 24.2.

After shutdown, all of the plasma calorimeters were removed from the target chamber and recalibrated, with some rebuilt for return to service. A full complement of 20 calorimeters will be operational during the next experimental campaign. Two new auxiliary vacuum pumps have been installed, increasing the roughing speed for the main target chamber by a factor of 2, and providing increased capability for peripheral vacuum diagnostics. A new task scheduler has been implemented in the experimental control room, allowing computer control of various control functions such as fast and slow timing, film advance, vacuum control, high voltage, and oscilloscope camera control.

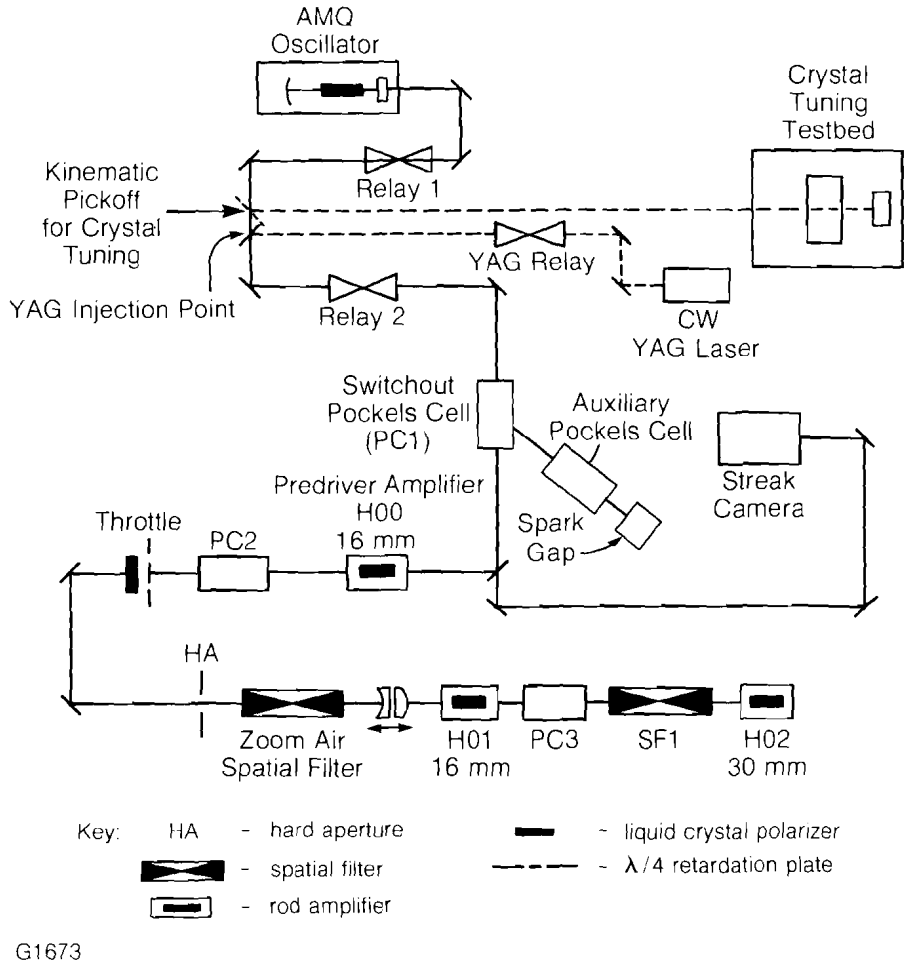

Fig. 24.2
Diagram of the OMEGA driver line, including the new AMQ oscillator, switchout predriver amplifier, and zoom spatial filter.

Engineering of the 25th-beam project is near completion. Beam transport components and frequency conversion supports are being installed, with the anticipated completion date in mid-October. The communications protocol, which allows control of the GDL laser from OMEGA control, will be tested at that time.

ACKNOWLEDGMENT

This work was supported by the U.S. Department of Energy Office of Inertial Fusion under agreement number DE-FC08-85DP40200 and by the Laser Fusion Feasibility Project at the Laboratory for Laser Energetics which has the following sponsors: Empire State Electric Energy Research Corporation, General Electric Company, New York State Energy Research and Development Authority, Northeast Utilities Service Company, Ontario Hydro, Southern California Edison Company, The Standard Oil Company, and University of Rochester. Such support does not imply endorsement of the content by any of the above parties.

Section 2
PROGRESS IN LASER FUSION

2.A High-Aspect-Ratio Laser-Fusion Targets Driven by 24-Beam UV-Laser Radiation

The compression of spherical, DT fuel pellets to high densities is achieved by depositing laser light on the surface of the target to create a high-temperature, ablating plasma. Many experimental and theoretical studies have established the advantages of short-wavelength laser irradiation for the effective coupling of laser energy into a high-density collisional plasma[1-5] (without the generation of copious suprathermal electrons[5-6]) and for the generation of high ablation pressures[7] sufficient to drive an efficient compression on a low isentrope. From simple heuristic arguments,[8] and from the predictions of two-dimensional (2-D) hydrodynamic simulations,[9] implosion uniformity of spherical-shell targets to high final-core densities under direct multibeam laser irradiation will be maintained only for modest initial shell-aspect-ratios $[(R/\Delta R)_o]$ under a high degree of illumination uniformity.

Low-aspect-ratio targets will be used in future high-density experiments on OMEGA. However, the first set of UV implosions were performed with high-aspect-ratio targets because they were predicted to produce the relatively high neutron yields needed to checkout diagnostics, which measure the fuel and shell areal densities. Computer simulations show that the high yield is produced, in part, by a strong shock that propagates through the fuel and preheats it. (However, the shock preheat also limits the amount of fuel compression.) The calculations also show that the initially high aspect ratio is, in fact, substantially reduced early in the implosion due to expansion of the shell from radiative preheat, making the target less vulnerable to disruption by

the Rayleigh-Taylor instability. The targets used were relatively large, resulting in low peak intensities ($< 2 \times 10^{14}$ W/cm^2); this minimizes the generation of fast electrons from parametric processes,[10] simplifying the modeling of thermal energy transport within the target.

The experiments discussed in this report were made with large-diameter, large-aspect-ratio [$(R/\Delta R)_0 \sim 300$], DT-filled glass microballoons. A large number of plasma, x-ray, and nuclear diagnostics were deployed to characterize the coronal plasma, the hydrodynamics of the implosion, and the final compressed core conditions. These included a time-resolving x-ray streak camera[11] and a transmission grating,[12] x-ray spectroscopy and photography,[13] and neutron time-of-flight spectrometry.[14] The measurement of the fuel and shell areal densities was made using fuel ion (knock-on) spectrometry[15] and neutron activation,[16] respectively. Simulations of these experiments were made with the one-dimensional (1-D) hydrodynamic code, *LILAC*,[17] which includes inhibited thermal transport, LTE radiation physics, and laser energy deposition via a ray-tracing algorithm in the underdense plasma. Neutron yields in these experiments were as high as 2×10^{11}, the highest so far reported for any laser-fusion experiments.[18]

Hydrodynamic simulations of these thin-walled, large-diameter glass microballoon targets give considerable insight into the characteristics of the implosion. The predicted behavior of a characteristic target is shown in Figs. 24.3 and 24.4. The target was a glass microballoon, ~ 750 μm in diameter, containing 10 atm of DT gas, with a wall thickness of ~ 2 μm. It was irradiated with 2 kJ of 351-nm radiation in 700 ps (average intensity $\sim 1.83 \times 10^{14}$ W/cm^2). Although $(R/\Delta R)_0 = 185$, it can be seen from Fig. 24.3(b) that the effective-aspect ratio decreases rapidly during the acceleration phase of the implosion and has decreased to ~ 20 at the half-radius point. Figures 24.3(c) and 24.3(d) show that the majority of the energy is absorbed during the first half of the implosion; 83% of the total absorbed energy is deposited by the time the maximum implosion velocity (5×10^7 cm/s at the fuel-glass interface) is reached. The peak intensity in the absorption region, specifically at the critical density surface ($n_c \sim 10^{22}$ cm^{-3}), never exceeds 1.0×10^{14} W/cm^2 [Fig. 24.3(d)], which is below the values expected for the onset of parametric instabilities producing suprathermal electrons. The predicted 1-D time histories for neutron production, DT ion temperature and density, and fuel and shell areal density are shown in Figs. 24.4(a) through 24.4(d), respectively. The neutron generation in Fig. 24.4(a) commences on the convergence of the first shock, which propagates with a velocity greater than 5×10^7 cm/sec. The average DT ion temperature and density rise to maximum values of ~ 6 keV and ~ 0.7g/cm^3, respectively [Fig. 24.4(b)], at the time of maximum compression. At this point in the implosion, the fuel and shell areal densities have risen sharply to the maximum values indicated in Figs. 24.4(c) and 24.4(d). The 1-D neutron yield for this simulation is 2.4×10^{12}.

The actual implosion experiments used DT-filled (10 atm), 700- to 800-μm-diameter glass microballoon targets with wall thickness in the

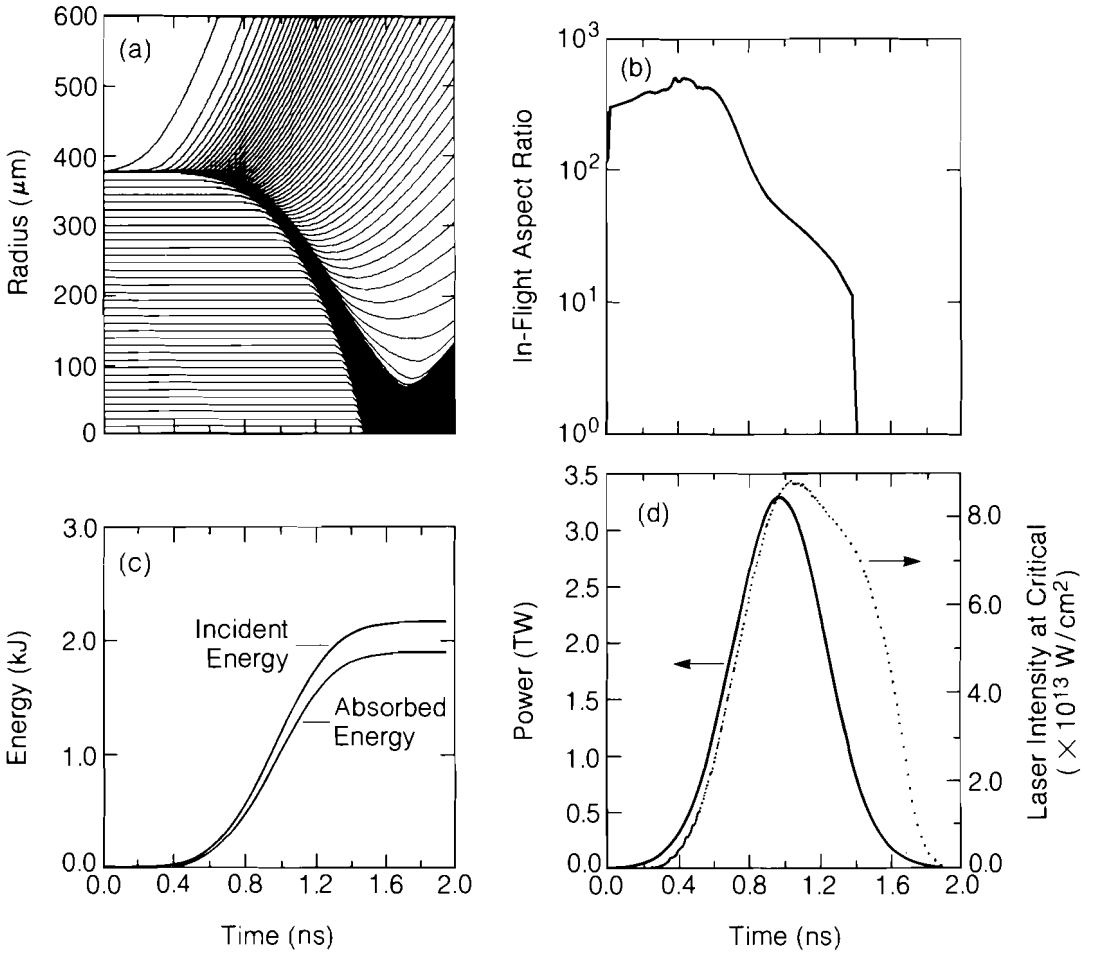

Fig. 23.3
One-dimensional LILAC *simulations of the implosion of a DT-filled (10 atm), 700-μm-diameter, 2-μm-wall glass microballoon irradiated with a 2-kJ, 700-ps pulse of 351-nm laser light:*
(a) radius-time (R-t) plot of the Lagrangian elements;
(b) in-flight-aspect ratio;
(c) time-integrated laser absorption; and
(d) intensity at the critical surface as a function of time during the implosion.

range of 1.3–2.1 μm, and were performed using the newly up-converted 24-beam OMEGA laser system.[18] The beams were focused on target with 600-mm-focal-length (f/3.7), single-lens optics. Up to 2.4 kJ of 351-nm laser radiation was delivered to the target in a 700-ps pulse (FWHM), with a 3% beam energy variance. The individual beams had lateral and axial positional accuracies of 10 and 50 μm, respectively. They were focused to various positions beyond the target center, in order to vary the degree of beam overlap and illumination uniformity. From a characterization of the intensity distribution in the

target plane, a minimum level of illumination nonuniformity of 16% rms was estimated for a focus of 10 target radii (F = 10R) beyond the target center. These targets, irradiated with an average intensity of 2×10^{14} W/cm^2, had an estimated peak-to-valley intensity variation of 60%. The overall absorption, measured with an array of differential plasma calorimeters, was 80%, and, to within 5%, was invariant for focal positions between F = 4R to 9R. Measurements of the continuum x-ray emission spectrum indicated, as with earlier 6-beam experiments on solid spherical targets,[5] that $< 10^{-4}$ of the absorbed energy was coupled to collisionless suprathermal electrons.

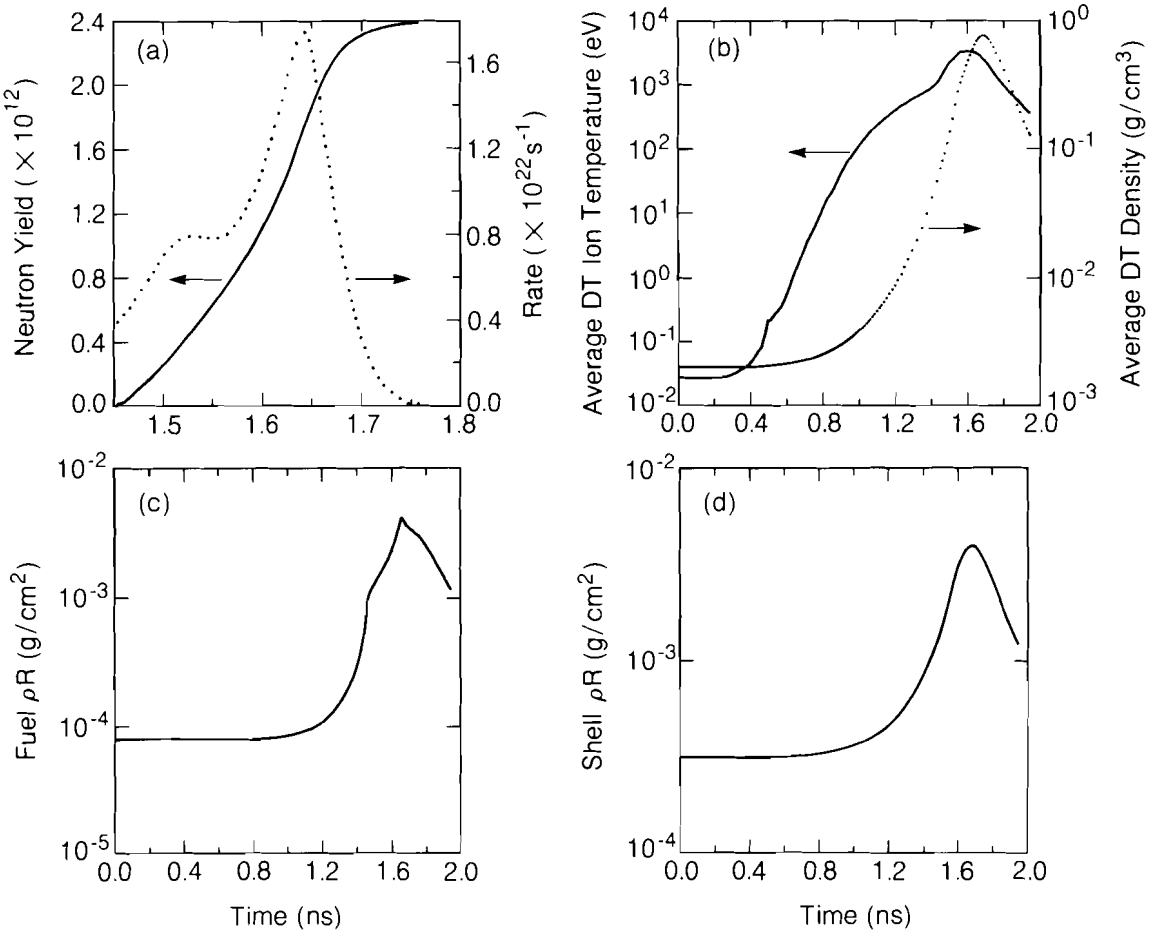

Fig. 24.4
Calculated time histories of target conditions during the implosion:
(a) integrated neutron yield and neutron production rate;
(b) mass-averaged fuel-ion temperature and fuel density;
(c) average fuel areal density; and
(d) average shell areal density.

Several diagnostic systems were deployed to determine the hydrodynamics and final core conditions of the imploding target. Time-integrated x-ray photography, with either a pinhole camera (x-ray energy E ~ 2 keV) or a Kirkpatrick-Baez microscope (E ~ 4 keV), spatially resolved the x-ray emission from the imploding shell. Figure 24.5(a) shows a plot of contours of a constant film x-ray exposure as determined from such an x-ray micrograph. The image contains a central region of emission, ~120 μm in diameter. This feature is the result of x-ray emission from the inside wall of the shell, which is heated in the final stages of the implosion — initially by the outward-going reflected shock in the compressed fuel, and finally by electron thermal conduction from the hot fuel to the shell. The azimuthal average of this image about the implosion center [Fig. 24.5(b)] indicates that the average radius of the emitting region was ~50 μm at the time of peak emission. The corresponding simulation of the x-ray micrograph by the hydrodynamic code *LILAC* [Fig. 24.5(b)] shows an emission region of approximately the same size produced by the stagnating shell.

Measurements of the fuel and shell areal densities were made using knock-on fuel-ion spectrometry[15] and neutron activation of ^{28}Si, respectively. These techniques probe the compressed target conditions

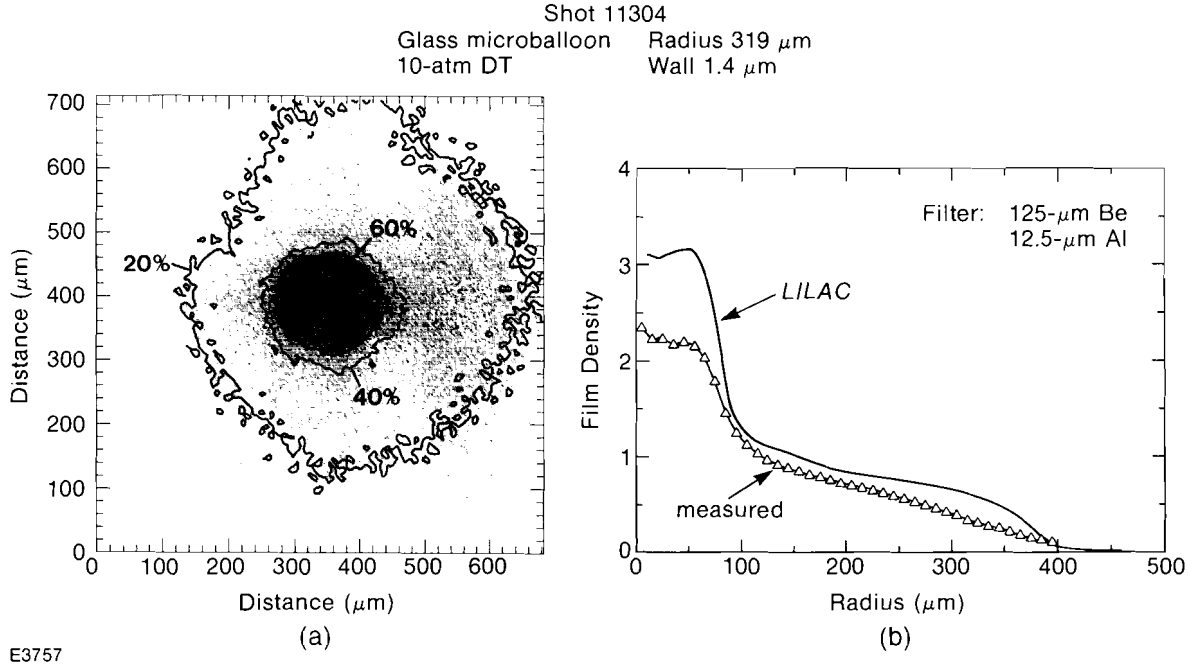

Fig. 24.5
Details of a 4-keV micrograph of x-ray emission from the target.
(a) 2-D contour plot of the x-ray intensity overlaid on a density-shaded reduction of the x-ray micrograph;
(b) azimuthally averaged x-ray intensity deduced from (a), compared to the predicted x-ray intensity from the hydrodynamic code LILAC.

at the time of maximum neutron generation. The shell ρR was measured using the number of $^{28}Si(n,p)\ ^{28}Al$ reactions (cross section $\sigma = 0.25b$) induced in the imploded glass shell, by detecting[19] the coincident 1.78-MeV γ-ray and 2.86-MeV β-particle decays of ^{28}Al (half-life 2.25 min). A small fraction ($\eta_c \sim 0.8\%$) of these particles was collected by a thin (50-μm) Ti cone collector and rapidly extracted from the target chamber with an automatic extraction and collection system.[20] The number of activations N_c^* initially counted is related to the neutron yield (Y_n) and the average shell area density $<\rho\Delta R>$ by $N_c^* = k_c Y_n <\rho\Delta R>$, where k_c includes η_c, σ, and factors accounting for the counting duration and the delay between activation and onset of counting. To exceed the threshold level of measurement in these experiments, defined as 10 recorded counts in 5 min (background level ~ 1 count/1.2 min), the required $Y_n <\rho\Delta R>$ product must be $\gtrsim 10^7$ neutrons g/cm^2.

The average fuel $<\rho R>$ was estimated from the number of deuterons and tritons scattered by the 14.6-MeV DT neutrons in the compressed fuel. A fraction of these was detected by thin (100-μm) CR-39 nuclear track detectors deployed in Ta-filtered, gas-filled cells (to reduce background tracks); the detectors subtend a maximum solid angle of $\sim 1\%$. The number of coincident tracks[15] (N_T^*) on both sides of the etched CR-39, produced by the scattered deuterons and tritons, is directly related to Y_n and to the average fuel ρR by $N_t^* \sim k_t Y_n <\rho R>$, where k_t includes the collection fraction and the fraction of the total scattered ion distribution recorded by the track detector. For $<\rho R>$ values less than $\sim 4 \times 10^{-3}$ gm/cm^2, the latter is constant, as the thin imploded shell will not distort the spectrum of scattered deuterons and tritons.[21] (With several of these detectors deployed around the target, inferences about the uniformity of the compressed core could be made.) For a counts/background ratio of 10, and an ion collection fraction above 1% of the total solid angle, the required $Y_n <\rho R>$ product is $\sim 10^6$ neutrons g/cm^2.

The measured neutron yield as a function of the focus parameter for two-diameter ranges of thin-wall glass microballoon targets is shown in Fig. 24.6. The maximum yield (2×10^{11}) was found for $F = 4R$, a focus condition for which the 24, f/3.7 beams of OMEGA are contiguously focused on the target surface. This yield, however, is considerably lower (by a factor of 20) than that predicted [see Fig. 24.4(a)]. Some insight into the behavior of the target during the final stages of the implosion, when neutrons are produced, can be obtained by comparing the measured values of the neutron yield and the fuel and shell areal densities with those predicted by *LILAC* (Fig. 24.4 and Table 24.I). The measured values of Y_n, ρR, and $\rho\Delta R$ correspond to the predicted values of these parameters at a time of ~ 50 ps before the final stagnation, corresponding approximately to the time that the first compression wave reaches the center of the target and rebounds against the inside wall of the shell. After this time, it is possible that hydrodynamic instabilities disrupt the shell during the final stage of the implosion. The interpretation of the implosion results is at present speculative, and requires further analysis of the experimental data.

- Maximum neutron yield generated for contiguous beam irradiation of target

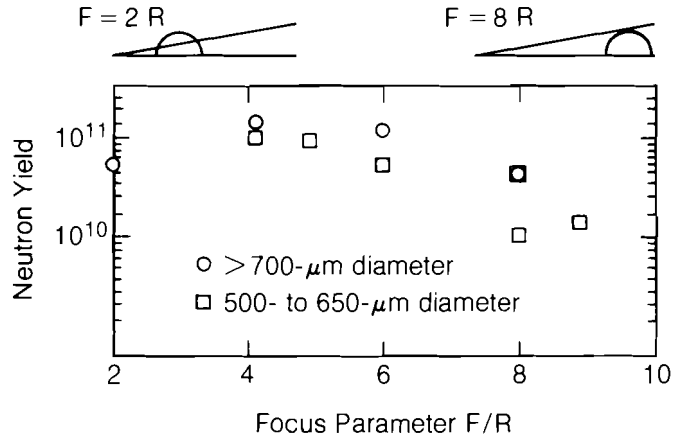

E3627

Fig. 24.6
Neutron yield versus laser-beam focus (in units of target radii behind the target center). Tangential focus corresponds to ~7.5.

Characteristic Experimental and Theoretically Predicted Compressed Core Parameters (Shot 11200)

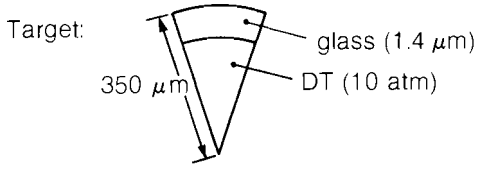

Laser: Energy = 2.2 kJ
Intensity = 2.3×10^{14} W/cm^2

	SIMULATION		EXPERIMENT	
	Total	First Compression		(No. of Counts)
Neutron Yield	1.2×10^{12}	1.5×10^{10}	2.7×10^{10}	($\sim 10^4$)
Fuel ρR	2.5×10^{-3} g/cm^2	9.1×10^{-4} g/cm^2	5.8×10^{-4} g/cm^2 $\pm 0.6 \times 10^{-4}$ g/cm^2	(120)
Shell ρR	3.2×10^{-3} g/cm^2	1.2×10^{-3} g/cm^2	1.1×10^{-3} g/cm^2 $\pm 0.1 \times 10^{-3}$ g/cm^2	(130)

E3756

Table 24.I.
Characteristic experimental and theoretically predicted compressed core parameters (shot 11200).

ACKNOWLEDGMENT

This work was supported by the U.S. Department of Energy Office of Inertial Fusion under agreement number DE-FC08-85DP40200 and by the Laser Fusion Feasibility Project at the Laboratory for Laser Energetics which has the following sponsors: Empire State Electric Energy Research Corporation, General Electric Company, New York State Energy Research and Development Authority, Northeast Utilities Service Company, Ontario Hydro, Southern California Edison Company, The Standard Oil Company, and University of Rochester. Such support does not imply endorsement of the content by any of the above parties.

REFERENCES

1. D. C. Slater *et al.*, *Phys. Rev. Lett.* **46**, 1199 (1981).
2. W. C. Mead *et al.*, *Phys. Rev. Lett.* **47**, 1289 (1981).
3. W. Seka *et al.*, *Opt. Commun.* **40**, 437 (1982).
4. C. Garban-Labaune *et al.*, *Phys. Rev. Lett.* **48**, 1018 (1982).
5. M. C. Richardson *et al.*, *Phys. Rev. Lett.* **54**, 1656 (1985).
6. R. L. Keck *et al.*, *Phys. Fluids* **27**, 2762, (1984).
7. B. Yaakobi *et al.*, *J. Appl. Phys.* **57**, 4354 (1985).
8. J. Nuckolls, L. Wood, A. Thiesson, and I. Zimmerman, *Nature* **239**, 139 (1972).
9. LLE Review **23**, 125 (1985).
10. A. Simon, R. W. Short, E. A. Williams, and T. Dewandre, *Phys. Fluids* **26**, 3107 (1983).
11. B. L. Henke and P. A. Jaanimagi, *Bull. Am. Phys. Soc.* **29**, 1388 (1984).
12. M. C. Richardson, R. S. Marjoribanks, S. A. Letzring, J. M. Forsyth, and D. M. Villeneuve, *IEEE Quant. Electron.* **QE-19**, 1861 (1983).
13. M. C. Richardson, S. A. Letzring, W. Friedman, and G. Gregory, *High-Speed Photography, Videography, and Photonics* (SPIE, Bellingham, WA, 1983), Vol. 427, p. 91.
14. S. A. Letzring, G. Pien, L. M. Goldman, M. C. Richardson, and J. M. Soures, *Bull. Am. Phys. Soc.* (to be published).
15. S. Kacenjar, S. Skupsky, A. Entenberg, L. Goldman, and M. C. Richardson, *Phys. Rev. Lett.* **49**, 463 (1982); S. Kacenjar, L. M. Goldman, A. Entenberg, and S. Skupsky, *J. Appl. Phys.* **56**, 2027 (1984).
16. E. M. Campbell *et al.*, *J. Appl. Phys.* **51**, 6062 (1980).
17. University of Rochester, LLE Report No. 16 (1976).
18. M. C. Richardson *et al.*, *Proceedings of 1985 Conference on Lasers and Electro-Optics* (IEEE, New York, 1985), p. 234.
19. S. M. Lane, E. M. Campbell, and C. Bennett, *Appl. Phys. Lett.* **37**, 600 (1980).
20. The collection efficiency of the Ti cone collectors, which subtended ~2% of the fuel solid angle, was estimated independently by measuring the ^{28}Si decay from activated empty glass microballoons.[16]
21. S. Skupsky and S. Kacenjar, *J. Appl. Phys.* **52**, 2608 (1981).

2.B Absorption Spectroscopy as a Diagnostic for Highly Compressed Targets

This article examines the possibility of using absorption spectroscopy as a compression diagnostic for high-density implosion experiments. Such experiments, planned for the 24-beam OMEGA UV laser, are of two kinds: (1) gas-filled targets designed to exceed compressions of 50 times liquid DT density, and (2) cryogenic fuel targets designed to exceed 200 times liquid DT density.[1] Some results for diagnosing the cryogenic targets are presented here.

Emission-line spectroscopy of fuel additives is not expected to be a suitable diagnostic for these high-compression experiments for several reasons. In glass-shell targets overcoated with plastic, the compressed glass shell significantly blocks emission lines from low-Z fuel additives (up to ~argon, Z = 18). If the fuel is seeded with higher-Z elements, the attenuation would be sufficiently low for resonance line emission from the most highly ionized species, but the low central temperatures required for high compression may not be adequate to produce these states of ionization in sufficient abundance. In addition, radiation by fuel additives can modify the implosion by cooling the compressed DT, so that the resulting compression is not indicative of the compression attainable with the same target filled with pure DT. It may in fact be impossible to fabricate cryogenic targets with fuel additives, since any impurities would condense out of the DT gas and freeze against the inner wall of the shell before the DT condenses.

With absorption spectroscopy, one measures the areal density (ρR) of the target shell using absorption features that have been impressed upon continuum radiation as it passes through the shell. The 1s-2p absorption transition in helium-like through fluorine-like ions form absorption lines whose total strength is nearly proportional to ρR of the absorbing material.[2] Such lines have been observed in KCℓ shell ions in implosion experiments at the Los Alamos National Laboratory (LANL) (see Fig. 24.7)[2] and have been observed in silicon ions from ablative implosions performed at LLE.[3] These absorption lines provide a spectral signal, at relatively high photon energies (a few keV), from ions in a relatively cool (Te ~ few × 100 eV) environment. The continuum-absorption processes can also shape the emission continuum in a ρR-dependent fashion.

The usefulness of these absorption effects are examined using non-LTE simulations of spectra calculated with an atomic rate-equation radiative-transfer code, together with 1-D hydrocode (*LILAC*) calculations of the high-compression implosions. The absorption features are examined for several variations of the same target. The simulated spectra show roughly what diagnostic capabilities are required, including temporal resolution, spatial resolution, and sensitivity.

In obtaining the spectrum simulations, atomic populations for all ionization species are calculated by solving time-dependent rate equations. The populations are used to calculate non-LTE opacities and

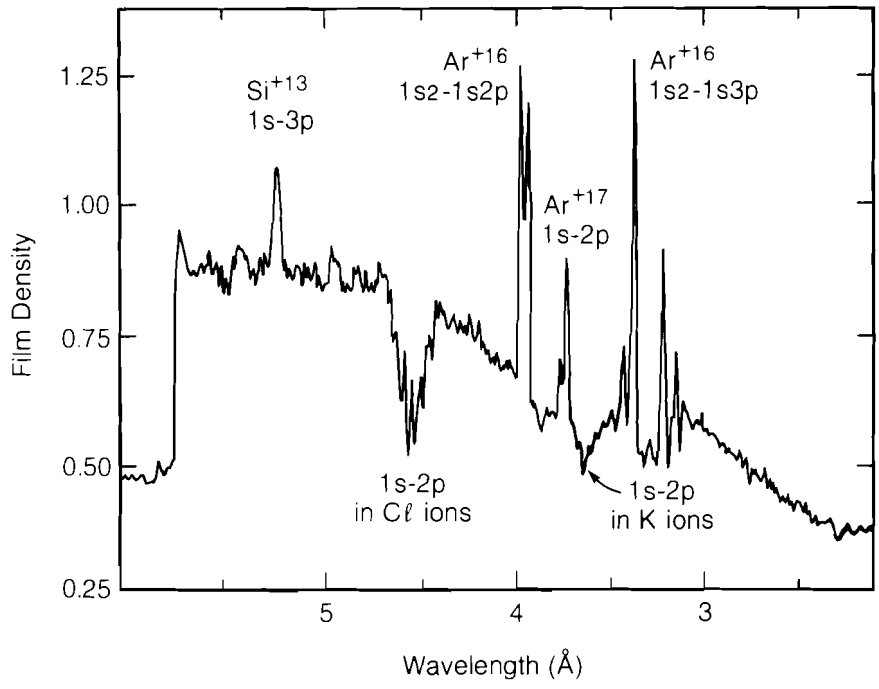

Fig. 24.7
Absorption lines due to a KCℓ layer in a CO_2-laser-imploded target consisting of a glass shell with KCℓ and CH coatings and a DT-plus-argon (1%) fill. This figure was provided by Allan Hauer of LANL.[2]

emissivities, and the resultant radiation is transported out of the target. Simple analytic expressions for the atomic energies and rates are used, many based on the screened-nucleus hydrogenic-ion model that includes tabulated line profiles and continuum lowering.[4] Distinct excited-state populations are calculated for the hydrogen-like and helium-like species, and only ground-state populations are kept for each remaining degree of ionization.

The determination of the shell ρR from absorption lines is based on the photoexcitation cross section per unit frequency interval

$$\sigma_\upsilon = \sigma L(\upsilon), \tag{1}$$

where σ is the total cross section

$$\sigma = (\pi e^2/mc)f, \tag{2}$$

f is the absorption oscillator strength, and $L(\upsilon)$ is the normalized line profile

$$\int L(\upsilon)d\upsilon = 1. \tag{3}$$

The attenuation of intensity I_o passing through the shell is given in terms of the shell ρR by

$$I(\upsilon) = I_o \exp(-\alpha\sigma_\upsilon \rho R/M_i), \tag{4}$$

where α is the fraction of all ions in the absorbing state and M_i is the mean ion mass. The ρR is then given by

$$\rho R = (M_i/\alpha\sigma) \int \ell n \left[I_o/I(\upsilon)\right] d\upsilon. \quad (5)$$

If the instrument response is logarithmic, then the integral is simply the area within the line, below the background continuum level. Note that the integration in Eq. (5) [together with Eq. (3)] eliminates the line profile $L(\upsilon)$ from the determination of ρR. Non-LTE computer simulations can be useful in interpreting experimental spectra when complications such as foreground emission must be taken into account or when estimates of the size and the spatial and temporal extent of the absorbing species are needed.

Results of Computer Simulations

A representative cryogenic target is shown in Fig. 24.8. It consists of a cryogenic DT layer inside a CH_2 shell, with the option of using a middle layer of glass. The calculated fuel compression exceeds 200 times liquid density when imploded by the 2-kJ pulse shown. The

Fig. 24.8
The layer-boundary trajectories of a representative high-compression target imploded by a 2-kJ pulse. The total hard x-ray emission from this implosion is plotted as both a time-resolved and spatially resolved signal against the radius and time axes of the layer-boundary trajectory plot.

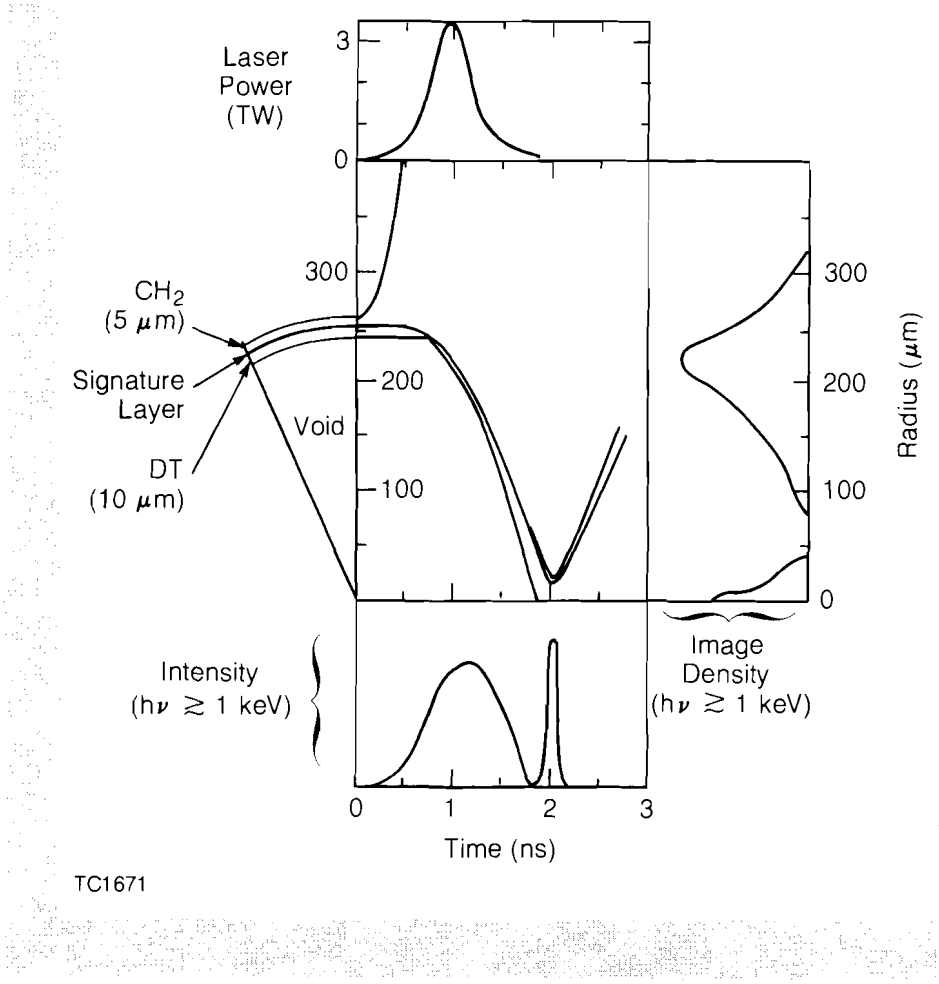

bottom plot of x-ray emission (> 1 keV) versus time shows a distinct separation of about 100 to 200 ps between the emission from the laser-heated ablation region in the CH_2 layer and from the core at peak compression. All the spectra from cryogenic targets shown in this article will be time integrated over the compression peak. Experimentally, this assumes a time-resolution capability of rejecting the ablator emission up to about 200 ps before the compression emission begins. As can be seen in the plot of time-integrated, spatially resolved emission at the far right of the figure, the compression emission can also be isolated by masking the image with a circular aperture roughly 60 to 100 μm in diameter. The glass shell can be doped with an additive to produce the desired absorption lines, or it can be replaced entirely with another signature layer.

The first signature layer to be considered is 1-μm thick, consisting of glass mixed with a 1% calcium impurity (all concentrations in this article are given by atom percent). Calcium is often a naturally occurring impurity in glass. The temperature and density profiles in this layer at peak compression are shown in Fig. 24.9 and are sufficient to ionize the

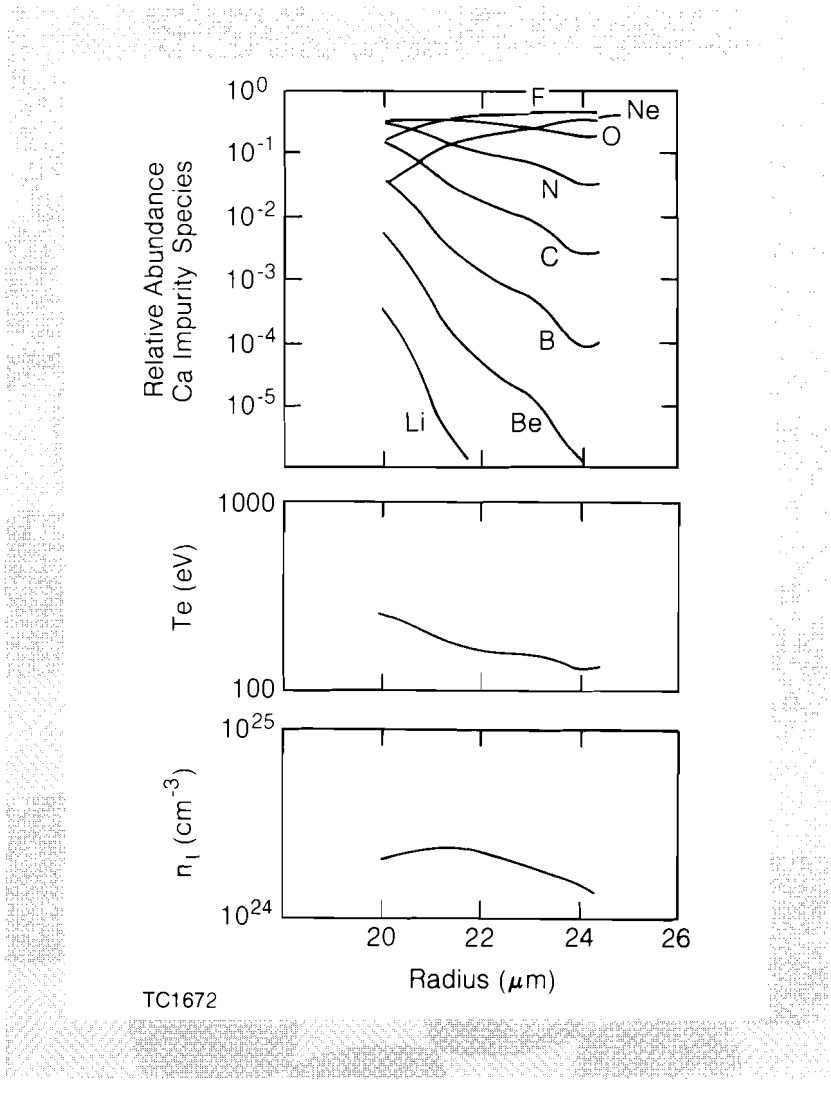

Fig. 24.9
Conditions in the glass shell at peak compression of a cryogenic target.

calcium impurity to beyond the fluorine-like species. The absorption lines from the 1s-2p transition are formed by all species from fluorine-like through helium-like. For calcium, these transitions occur at energies sufficiently high (3.7–3.9 keV) that the line absorption is not obscured by continuum emission in the glass.

The 1s-2p absorption transition is illustrated in Fig. 24.10 in the context of the simple atomic model used in the simulation. The two examples are the helium-like and boron-like species. The transition energies for each species and for each initial configuration of the n = 2 shell are nearly the same because the electron orbits are only slightly perturbed by adding electrons to the n = 2 shell. For the case of calcium, the shift in transition energy is only about 25 eV between successive species.[5] This small shift suggests that the initial and final electron orbits are fairly similar from species to species and that the transition matrix elements likewise ought not to change by a large

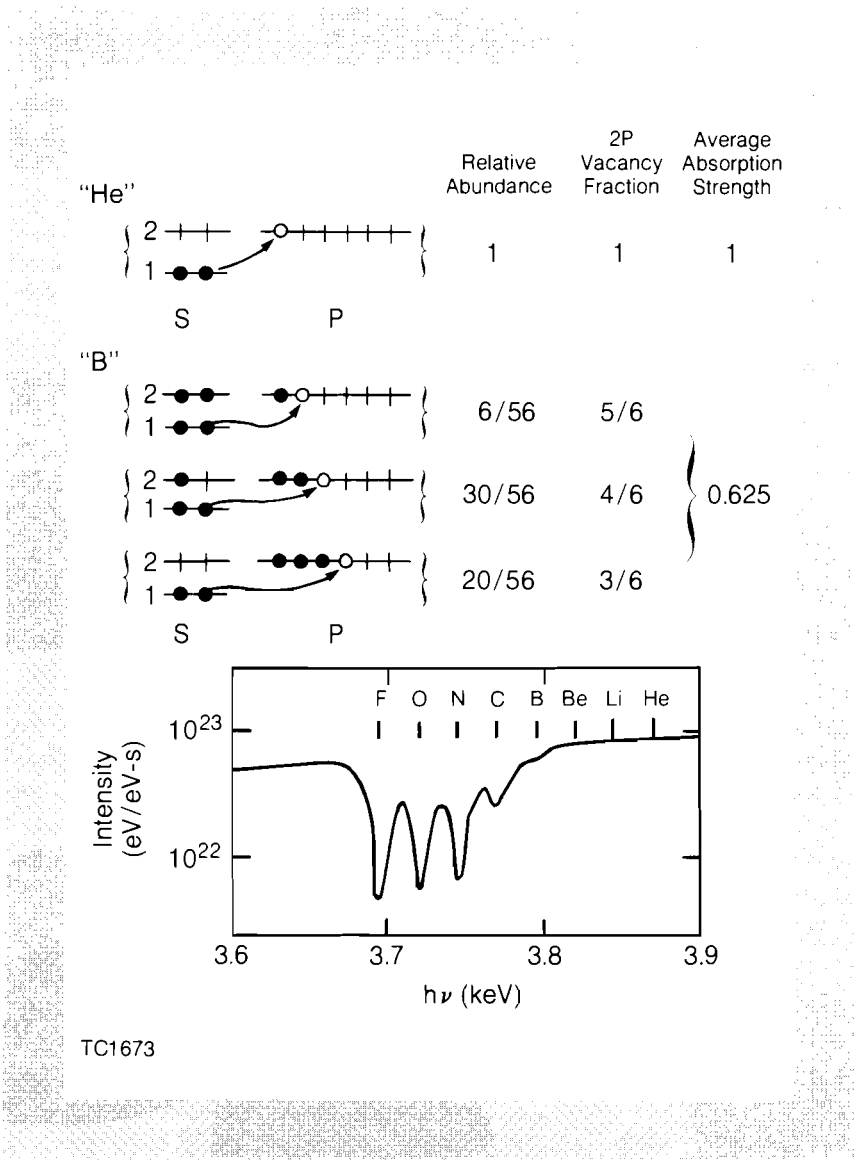

Fig. 24.10
An illustration of the K-shell (1s-2p) process that forms the series of absorption lines for the proposed diagnostic. The inset is a detail of the spectral intensity from the glass-shell target at the point in time depicted in Fig. 24.9.

amount. The approximation used is that the absorption cross section for each species is the cross section for the helium-like species with a factor accounting for the reduced vacancy fraction of the 2p shell as it fills. The cross section of each species is a statistically weighted average over the possible partitionings of $n=2$ electrons among the 2s and 2p shells in the initial state. In the simple atomic model used, the 2s and 2p levels are treated as degenerate. In reality, the 2s shell is filled first because of its lower energy, leaving the 2p shell more open, so the average cross section for each species is slightly larger than the average used here. As a consequence, the approximation used underestimates the intensity of the absorption line and is, in this one respect, conservative. For the example of the boron-like species, one can average the 2p-shell vacancy fractions over the relative statistical weights given for the respective initial configurations. The result is that the average 2p vacancy fraction is 0.625, so that the average absorption strength per ion for that species is 0.625 relative to the absorption strength for the helium-like species.

The spectrum at the bottom of Fig. 24.10 is the simulated spectral intensity for the glass-shell target at the time depicted in Fig. 24.9. The intensities of the absorption lines reflect the relative abundances of the corresponding species. Due to limitations in the current version of the simulation code, the absorption lines for each species will be superimposed at the same line energy using the helium-like line profile in all the simulations to follow. Even though the multiple-component structure will not be depicted, the total 1s-2p absorption due to all species will be accurately represented.

As a second example, we consider layers of argon and neon, condensed out of the fill gas against the inner-shell surface of a cryogenic target. They show the same absorption transition as the calcium impurity in the glass shell, but the shell transparency gained by removing the glass gives a much stronger signal. Figure 24.11 shows the initial configuration of the target with the glass-free signature layer. Spectra obtained assuming neon and argon fuel additives are compared with the spectrum obtained for a target with no signature layer. While the argon absorption line is very distinct, the neon absorption line is at a low enough energy to be blocked by the continuum opacity of the CH_2 shell.

For the purpose of this article, a time-integrated spectral intensity of 10^{13} can be taken as a state-of-the-art threshold sensitivity, with 10^{14} being a level where the shape of the spectrum can be seen. Such thresholds are difficult to estimate, and they do not anticipate future improvements in sensitivity. Possible approaches to improved sensitivity may involve large dispersing crystals in focusing geometries, such as in the von Hamos geometry.[6]

Another example of a glass-free shell is illustrated in Fig. 24.12. The spectrum is from a target with a $KC\ell$ signature layer placed within the CH_2 shell. Absorption lines from both potassium and chlorine are seen. For comparison, the bottom spectrum from the glass-shell target shows the calcium absorption line at a very low intensity. At present, this particular glass-shell target is probably not diagnosible with x rays,

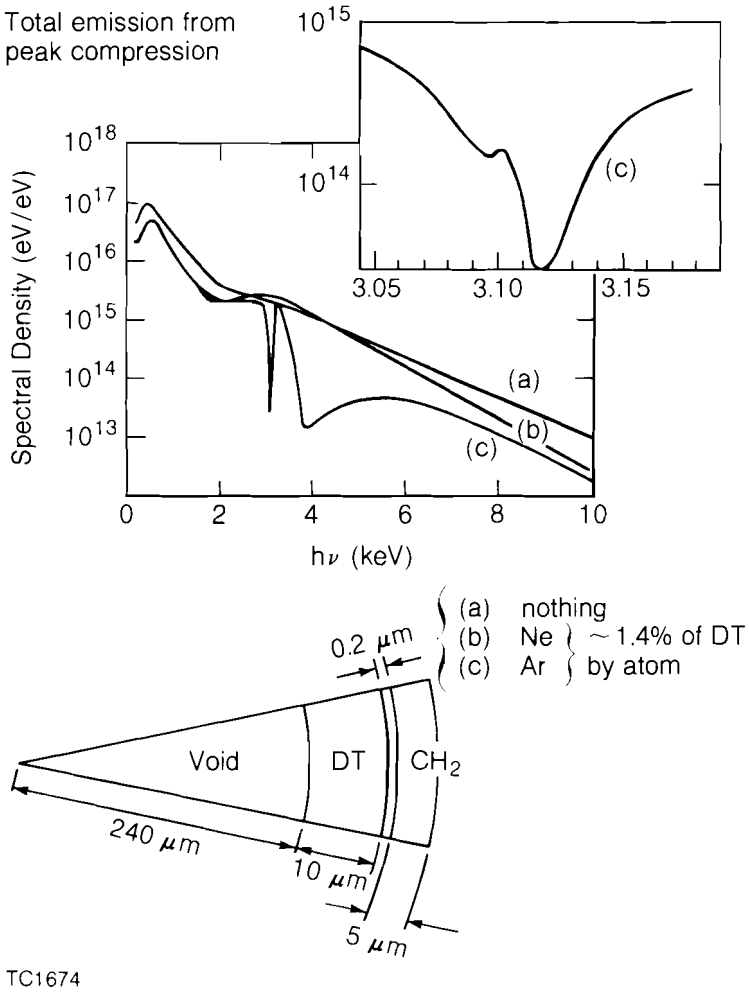

Fig. 24.11
Effects of fuel additives on the spectrum of a cryogenic target.

unless it does not perform as predicted by 1-D hydrodynamic simulations.

The minimum of the glass-shell intensity—near 3 keV—occurs at the energy at which the bound-free optical depth of the glass becomes small enough to allow the harder continuum from the DT to appear over the optically thick continuum of the cooler glass. The position of this minimum is another indication of the ρR of the glass shell. At the same time that the optical thickness of the glass obscures the absorption line, it provides, at least in principle, another absorption feature that is sensitive to the ρR of the shell.

The simulation of the glass-shell implosion was repeated with lower laser power in order to show how the absorption features change as the fuel and shell compressions are reduced. The resulting peak ρR values for these simulations are tabulated in Fig. 24.13. The corresponding spectra show that the point of inflection of the transmitted continuum

moves from 3 keV toward lower energies as the ρR of the shell decreases. At the lowest shell compression, the shell is thin enough to allow the K-edge and line absorption of silicon to appear. The total strength of the calcium line decreases with the shell ρR, and the profile of the line narrows as the peak density of the shell decreases. These trends can be explained qualitatively in terms of changes in the shell conditions at peak compression, but this perspective is somewhat oversimplified since the spectra are records covering hundreds of picoseconds, during which the target conditions are changing rapidly.

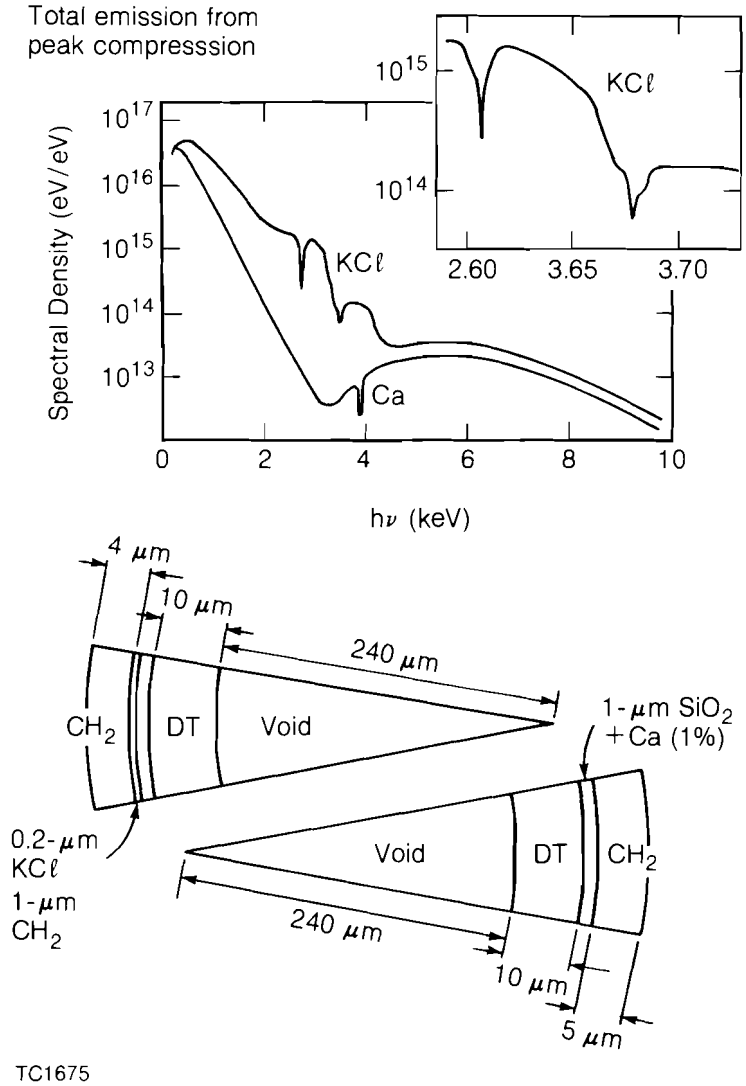

Fig. 24.12
Increased intensity with glass-free shells.

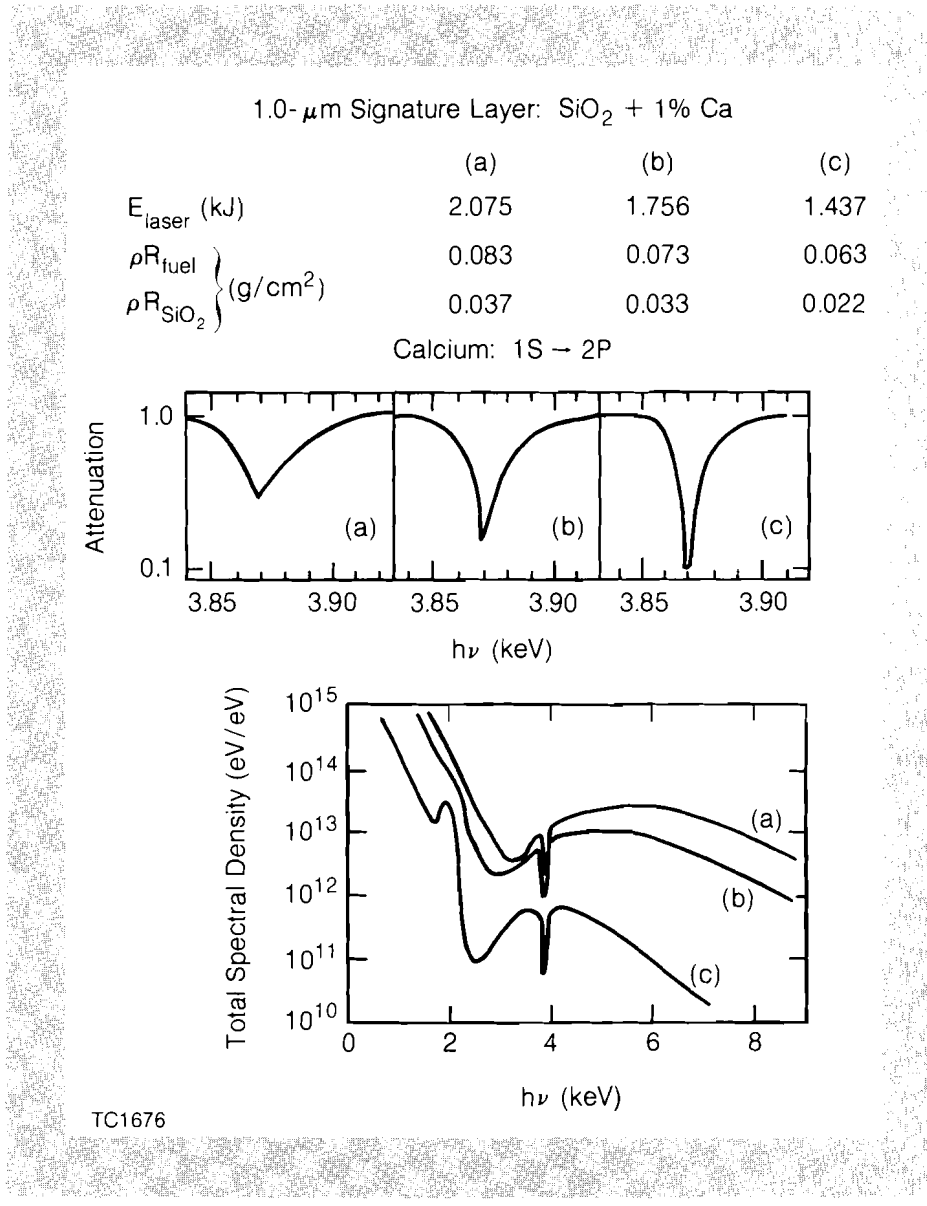

Fig. 24.13
Dependence of absorption features on target performance.

Mixing

In actual experiments, the targets considered here will not implode in the purely spherical mode of 1-D simulations. A combination of the nonuniformities in the laser illumination of the target and the Rayleigh-Taylor instability of the decelerating shell prior to peak compression may cause the shell to break up, resulting in compression conditions different from those predicted.[1] In the spherical simulations shown previously, the shell material remains relatively cool ($T_e \lesssim 200$ eV). If high-Z material from the disrupted shell mixes with DT that is heated to temperatures close to the predicted peak temperatures ($T_e \lesssim 1$ keV), then emission lines may appear as evidence that disruption has taken place.

The spectral signature of mixing has been obtained approximately by adding shell material to the DT as part of the initial conditions of the spectrum simulation. The same hydrocode information is used for this simulation as for the simulation without mixing so that the change of chemical composition is the only mixing effect modeled. At present, the non-LTE spectrum simulation can be performed only on 1-D simulations, which cannot model the hydrodynamics of mixing and the resulting time-dependent impurity concentrations.

Emission lines from shell material mixed into the hot DT must be of sufficient energy to penetrate the remaining intact shell. In the glass-free examples, lines from the hydrogen-like and helium-like species of argon, potassium, or chlorine in the DT penetrate the shell, but neon lines do not, unless the shell is severely thinned by hydrodynamic breakup. Simulations of the glass-shell target were obtained with the DT contaminated at a level of 1% by atom with shell material. The results are shown in Fig. 24.14. Curve (b) is obtained for the DT-shell mixture, which is to be compared with curve (a) obtained for a pure DT fill. Silicon features are seen at energies below the K-edge, where the glass shell is relatively transparent. Silicon Hα is emitted, and the Heα line is seen weakly in absorption. The shell transparency to these silicon features is marginal. In fact, the simulation shows that these features are blocked for about 150 ps, around the time of peak compression, when the ρR of the glass shell is above 0.02 g/cm^2 (peak ρR = 0.037 g/cm^2). These silicon features are very sensitive to the atomic

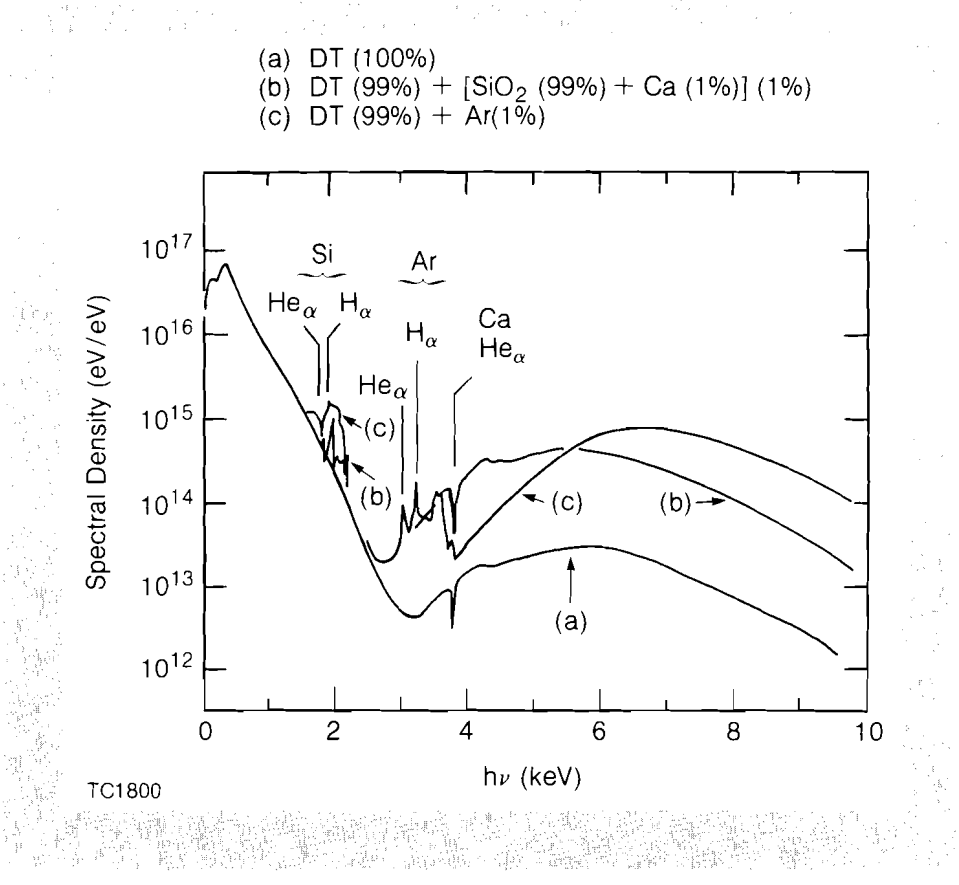

Fig. 24.14
Appearance of emission lines with fuel (DT) additives.

modeling. The same simulation performed with tabulated LTE opacities[7] for the glass shell shows no penetration of the shell by silicon lines. This can be explained with only a factor-of-two increase in the calculated opacity.

Curve (c) in Fig. 24.14 was obtained for an argon contaminant. The high-energy continuum is strongly enhanced, as in the shell-contaminated case. Argon 1s-2p lines are seen, although the glass attenuates them a great deal. The line-like structure near 4 keV is in part due to the superposition of ionization edges acting in emission and absorption. The line-like sharpness of these edges is an artifact of the uniformly layered structure of the target and of the simplified atomic model, which uses only a few ionization transitions to model ionic spectra.

The emission features in Fig. 24.14 are sensitive to the mixing depth. The temperatures in the spherical simulations are peaked in the center, and the emission features are not obtained if the contaminants are confined to the outer half of the fuel mass.

This discussion of mixing is necessarily preliminary because the spectrum simulations are based on ideally behaved implosion simulations with constant impurity concentrations. The development of diagnostics to detect shell disruption and other failure modes is an important goal that will require simulation studies using more realistic mixing models than the very simple one used here.

ACKNOWLEDGMENT

This work was supported by the U.S. Department of Energy Office of Inertial Fusion under agreement number DE-FC08-85DP40200 and by the Laser Fusion Feasibility Project at the Laboratory for Laser Energetics which has the following sponsors: Empire State Electric Energy Research Corporation, General Electric Company, New York State Energy Research and Development Authority, Northeast Utilities Service Company, Ontario Hydro, Southern California Edison Company, The Standard Oil Company, and University of Rochester. Such support does not imply endorsement of the content by any of the above parties.

REFERENCES

1. P. McKenty and C. P. Verdon, LLE Theory Group Report No. 15, 1985.
2. A. Hauer *et al.* (paper in preparation); LLE Review **22**, 51 (1985).
3. B. Yaakobi, R. L. McCrory, S. Skupsky, J. A. Delettrez, P. Bourke, H. Deckman, C. F. Hooper, and J. M. Soures, *Opt. Commun.* **34**, 213 (1980).
4. S. Skupsky, LLE Theory Group Report No. 11, 1979; R. Epstein, LLE Theory Group Report No. 13, 1984; R. Epstein, S. Skupsky, and J. Delettrez, *J. Quant. Spectrosc. Radiat. Transfer* (to be published).
5. L. L. House, *Astrophys. J. Suppl. Ser.* **18**, 21 (1969).
6. B. Yaakobi, R. E. Turner, H. W. Schnopper, and P. O. Taylor, *Rev. Sci. Instrum.* **50**, 1609 (1979).
7. W. F. Huebner, A. L. Merts, N. H. Magee, and M. F. Argo, Report No. LA-6760, 1977 (unpublished).

Section 3
ADVANCED TECHNOLOGY DEVELOPMENTS

3.A Ablation-Layer Coating of Mechanically Unsupported Inertial Fusion Targets

A high degree of target perfection is required to achieve optimum performance for inertial fusion implosions. Target design calculations indicate that nonuniformities in sphericity, concentricity, and layer thickness should be less than ~5% and that rms surface roughness should be less than ~1000 Å.[1] Typically, targets are supported using glass fibers or films, which constitute a significant departure from spherical symmetry and can contribute to hydrodynamic instability growth during implosion. Alternative target support schemes have been developed, e.g., spider webs or drawn glass fibers, to minimize the target mass perturbation.[2] Compared to conventional glass fiber stalks of 10-μm diameter, these mounts produce a thousandfold reduction in the effective target support mass and significantly improve target symmetry.[2] This improvement is defeated, however, if a target with a low-mass support is coated with an additional material that also coats and thickens the diameter of the support stalk. It is desirable to coat targets which are not mechanically supported, and afterwards to mount the low-mass support.

Various techniques have been employed for this purpose, including gas-jet levitation,[3] acoustic levitation,[4] and bouncing,[5] all with varying degrees of success. Most of the techniques have been discarded in favor of the bounce-coating method for a variety of reasons, one being that it is a batch process. The method has been mainly applied to ablation-layer coating using glow discharge polymerization schemes[5] that are not well understood. Another scheme, vapor-phase

polymerization of parylene, is a well established process for forming conformal thin films on any substrate,[6] and it is the process exclusively used for ablation-layer coating at LLE. This article describes the adaptation of the bouncing-pan scheme to ablation-layer coating by the parylene process.

Incorporation of the bounce-coating scheme to the parylene process is schematically illustrated in Fig. 24.15. The pyrolyzed 2,2-paracyclopane molecules are introduced to the region above the vertically vibrating pan, where targets are bouncing in a weak plasma (sustained with a power of ~10 mW). The primary purpose of the plasma is to neutralize the surface charge formed on the targets and thus prevent sticking and agglomeration of the targets. The plasma has an additional effect. Parylene monomers in the plasma can be changed into ions, radicals, and other energetic species, so that plasma polymerization may also proceed in addition to the parylene process. The polymerization suppresses crystallization and yields a smooth layer of deposited material. Before the coating process begins, Ar gas is introduced at a pressure of 0.1 Torr to allow the glow discharge to be started. As the pressure of parylene monomers increases, the Ar pressure is reduced to keep the total pressure constant. The pressure is adjusted to achieve a coating rate of 1 to 2 μm per hour, determined by an interferometric technique.[7]

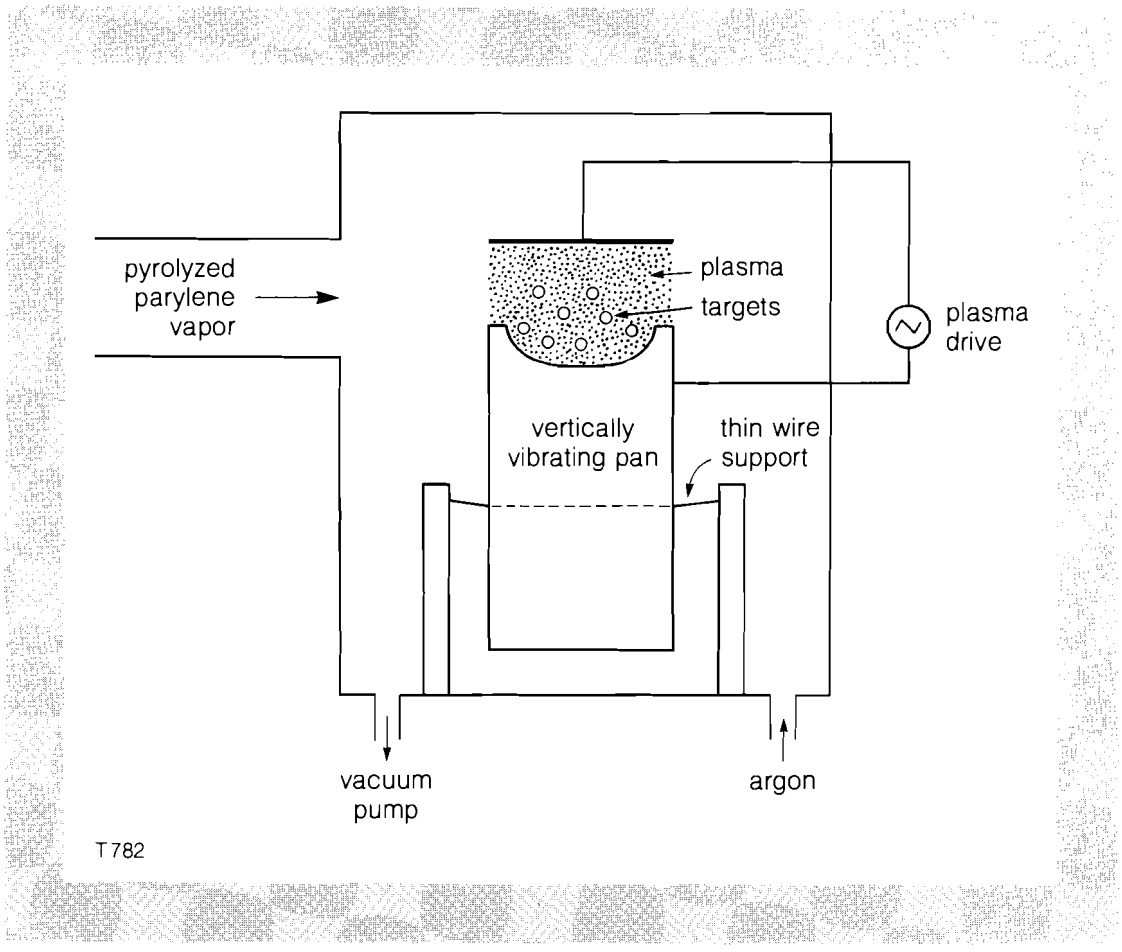

Fig. 24.15
Schematic of the bounce-coating process. Apparatus for sublimation and pyrolysis of the parylene is not shown.

To bounce targets successfully in a pan, it is important to be able to characterize the motion of all parts of the pan. If a pan of arbitrary shape is driven with a piezoelectric transducer, the system—consisting of pan, transducer, and connecting elements—responds with a unique set of vibrational modes. Each mode of vibration has regions of maximum and minimum motion, with amplitudes that are not readily predictable. In such a pan, the bouncing targets tend to stick at points of minimum motion. To overcome this problem, a system with predictable vibrational modes is needed.

A right circular cylinder has well characterized vibrational modes,[8–10] several of which are useful for bouncing targets. We employ a cylindrical resonator with a shallow pan shape machined into one end. The cylinder is suspended on thin wires, with its axis oriented vertically. A small piezoelectric strain transducer glued to the side of the cylinder excites a longitudinal mode of vibration. Modes with wavelengths larger than both the cylinder diameter and the pan depth have amplitudes that are reasonably uniform over the surface of the pan. In coating runs, we use the first longitudinal mode at a frequency of 16 to 20 kHz. There is no significance to this choice of frequency except that it is much higher than the bounce frequency of the targets, but much lower than the lowest mechanical resonant frequency of a target.[11] (25 Hz is used if the bounce height is 2 mm.)

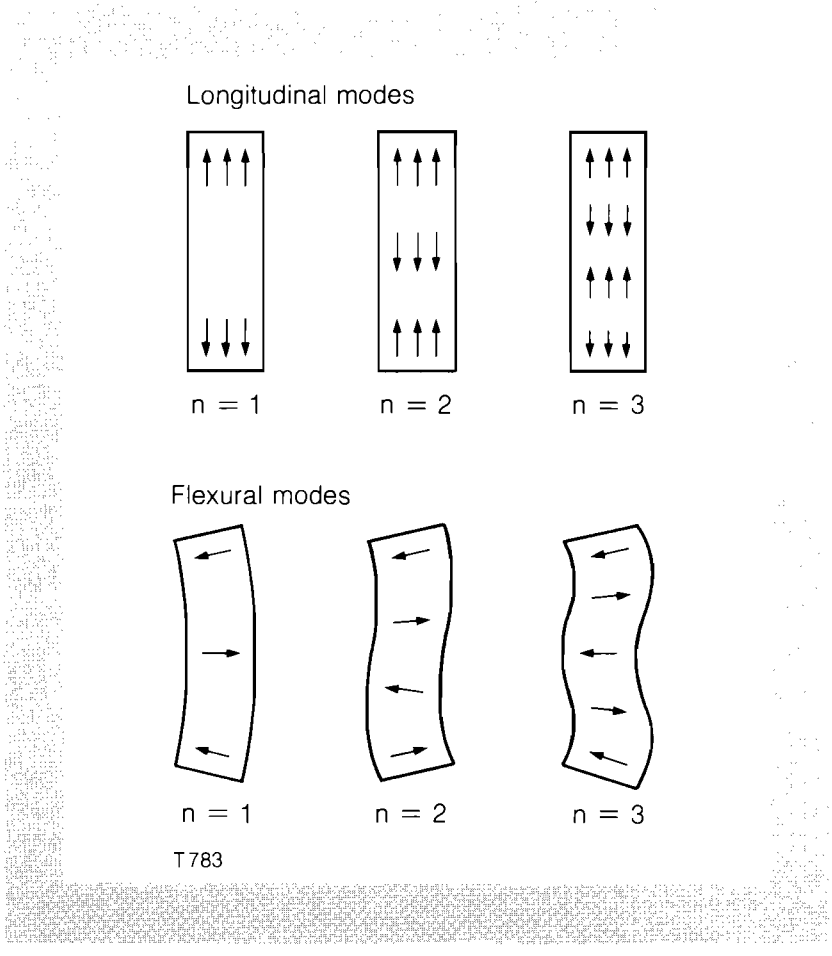

Fig. 24.16
Illustration of vibrational modes of a cylinder useful for bouncing targets or dislodging stuck targets. Arrows indicate the directions of motion of mass elements during half of a cycle.

In addition to employing the longitudinal mode for bouncing, we have investigated the use of flexural and torsional modes. Flexural modes were found to be particularly useful in unsticking targets before coating begins. After the targets are placed in the pan and a glow discharge is established, it is frequently observed that nearly all the targets are stuck to the pan with sufficient force that exciting the longitudinal mode to high amplitude fails to dislodge them. At this point, driving a flexural mode can dislodge them within seconds or minutes. Once dislodged, they can be bounced in the plasma, using longitudinal vibrations with little or no further sticking. Alternately, the targets may be left in the longitudinally vibrating pan with a glow discharge for several hours, after which most (though not necessarily all) will be bouncing.

The shapes of the vibrational modes are shown schematically in Fig. 24.16. The frequencies of these modes may be accurately predicted. Figure 24.17 shows how the frequencies of the modes vary with the ratio of diameter to length. This figure applies to materials with a Poisson's ratio of 0.333, characteristic of aluminum and its alloys. Cutting a pan shape into the end of the cylinder renders these predicted frequencies less accurate. Nevertheless, the predictions are

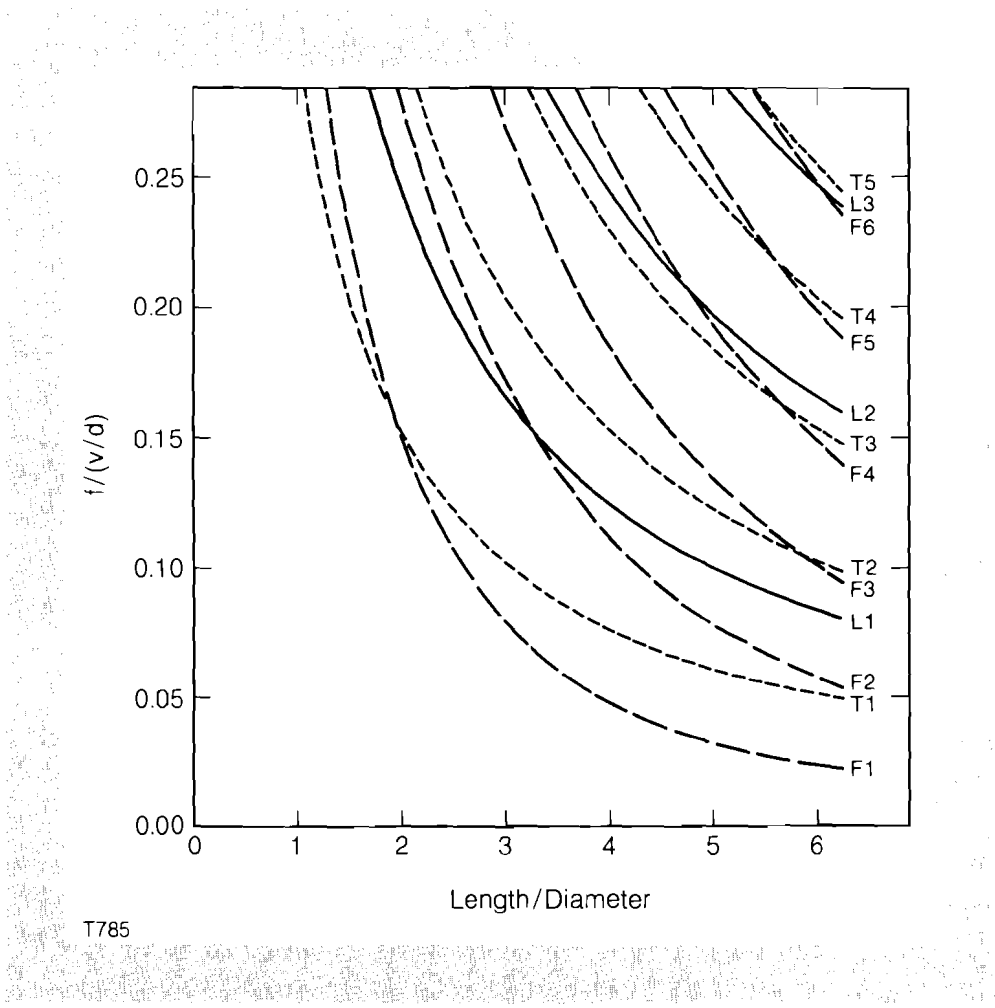

Fig. 24.17
Vibrational frequencies of a cylinder with Poisson's ratio = 0.333 as a function of its diameter-to-length ratio. The frequency f is expressed in units of v/d, where v = velocity of sound and d = diameter. The type of mode is denoted by L for longitudinal, F for flexural, or T for torsional, followed by the mode number.

still quite useful as approximations for helping to specify dimensions. Cylindrical dimensions are chosen so that no vibrational mode used for bouncing is close in frequency to another vibrational mode.

Longitudinal modes are characterized by displacement along the cylinder axis by an amount Δz given by

$$\Delta z \simeq \Delta z_0 \sin(2\pi f_{Ln} t) \begin{cases} \sin \dfrac{n\pi z}{\ell}, & \text{odd } n \\ \cos \dfrac{n\pi z}{\ell}, & \text{even } n \end{cases}, \tag{1}$$

where z is the distance along the axis from the center of the cylinder, ℓ = length of the cylinder, and Δz_0 is the peak amplitude. The frequency is given by

$$f_{Ln} \simeq \frac{nv}{2\ell}, \quad n = 1, 2, 3, \ldots, \tag{2}$$

where v is the velocity of sound. Equations (1) and (2) apply to long, thin cylinders. Corrections that depend on diameter and Poisson's ratio have been calculated.[8] Equation (1) is useful for choosing the positions of the support wires and the strain transducers. The cylinder is best supported where $\Delta z = 0$. The strain transducers are best placed at a region where the strain (the derivative of Δz with respect to z) is maximum. These principles are used to enhance some modes of vibration and to suppress others.

The flexural modes cannot be described with simple functions. Numerical solutions for their frequencies of motion are given in Refs. 9 and 10. It should be mentioned that each flexural mode is split into a pair of modes with perpendicular directions of motion and slightly different frequencies. We make use of both components, using a separate strain transducer for each.

Although torsional modes of vibration are potentially useful for moving targets, we have not yet coupled a strain transducer to these modes strongly enough to obtain more than slight target motion. These modes remain worthy of study, however, because unlike bending modes they produce pan motion perpendicular to the axis with no component along the axis.

The resonant pan is machined from a single piece of solid material with a high mechanical quality factor Q. By keeping the Q high, the drive transducer can be kept small and the driving signal can be kept at a low level. In addition, achieving a high value of Q minimizes the coupling between vibrational modes that happen to be close in frequency. Materials with an intrinsic $Q > 10^5$ at room temperature include several aluminum alloys such as 6061 and 5056 and some single crystals such as Si and Al_2O_3. In all of these materials, the value of Q increases as the temperature is reduced to cryogenic values, suggesting the possibility of doing coatings at cryogenic temperatures.

Because of the high value of Q, a vibrational mode cannot be maintained at a constant amplitude with an external oscillator. The temperature dependence of Young's modulus produces a fractional frequency change of -2×10^{-4} per °C in aluminum alloys, and a change in temperature of 0.1°C shifts the frequency by an amount greater than the width of the resonance. This problem is easily overcome by adopting a feedback scheme in which the resonant cylinder becomes the frequency control element of an oscillator. The feedback scheme, shown in Fig. 24.18, amplifies the signal from a detector strain transducer (which is identical to the drive transducer), filters out the signals associated with any unwanted modes, shifts the phase appropriately for driving the mode of interest, and provides some means of limiting the amplitude. Using this means to drive the first longitudinal mode, we have kept targets bouncing during coating runs that last many hours.

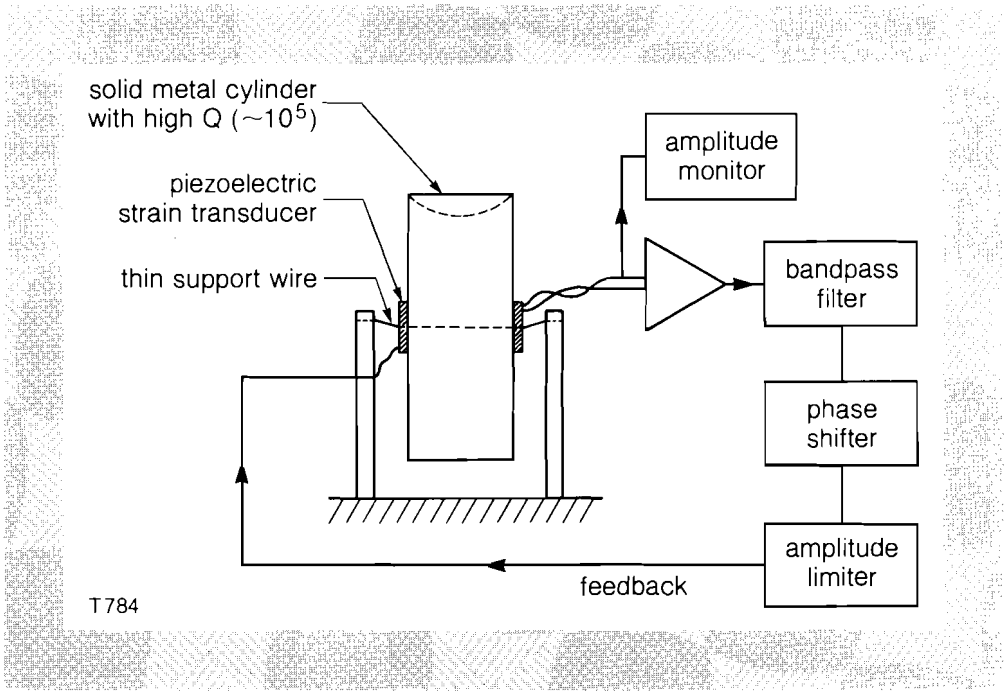

Fig. 24.18
Feedback circuit for maintaining a vibrational mode of a cylinder at constant amplitude.

A useful feature of the feedback scheme is the opportunity to constantly monitor the amplitude of pan motion and to calibrate the monitoring signal. The monitor is calibrated for a longitudinal mode by rigidly attaching a small, calibrated accelerometer to the bottom of the cylinder. The mode is excited by applying a signal to the drive transducer while comparing the resulting signals from the accelerometer and the detector transducer (both linear devices). The resulting calibration is expressed in volts at the strain transducer per unit acceleration of an end. One can then convert to velocity or amplitude by dividing acceleration by one or two powers of the angular frequency.

The pan velocity is chosen to try to maintain vigorous bouncing while not losing targets by bouncing them too high. A peak vertical pan velocity of ~34 mm/s is found to be suitable for bouncing glass microballoon targets of 400-μm diameter with a 1- to 2-μm wall. Under

these conditions, a wide distribution of bounce heights is seen, with the apparent average being several mm. After several microns of parylene are deposited, the targets bounce much higher and the peak pan velocity must be reduced by half to keep the average bounce height constant. We presume this phenomenon is related to the increased mass of the targets and to mechanical properties of the coating.

The quality of the ablation layer of targets coated by the present method has been investigated with a scanning electron microscope (SEM), and the results are shown in Figs. 24.19(a), 24.19(b), and 24.19(c). The surface smoothness is similar to that observed in the parylene coating of stalk-mounted targets.[12] Two methods can be applied to further improve the surface smoothness. The use of ethyl-substituted 2,2-paracyclopane instead of the nonsubstituted type has been shown to improve the surface smoothness.[12] No complications are expected in using ethyl 2,2-paracyclopane in the present experiment. The use of the low-power glow discharge should improve the surface quality of the coating, as mentioned previously. The plasma power is kept low, however, because—among other effects—film embrittlement occurs at higher plasma power and the film develops an amber color. The exact nature of the discoloring process is not known but it appears that the plasma may induce formation of color centers in the plastic.

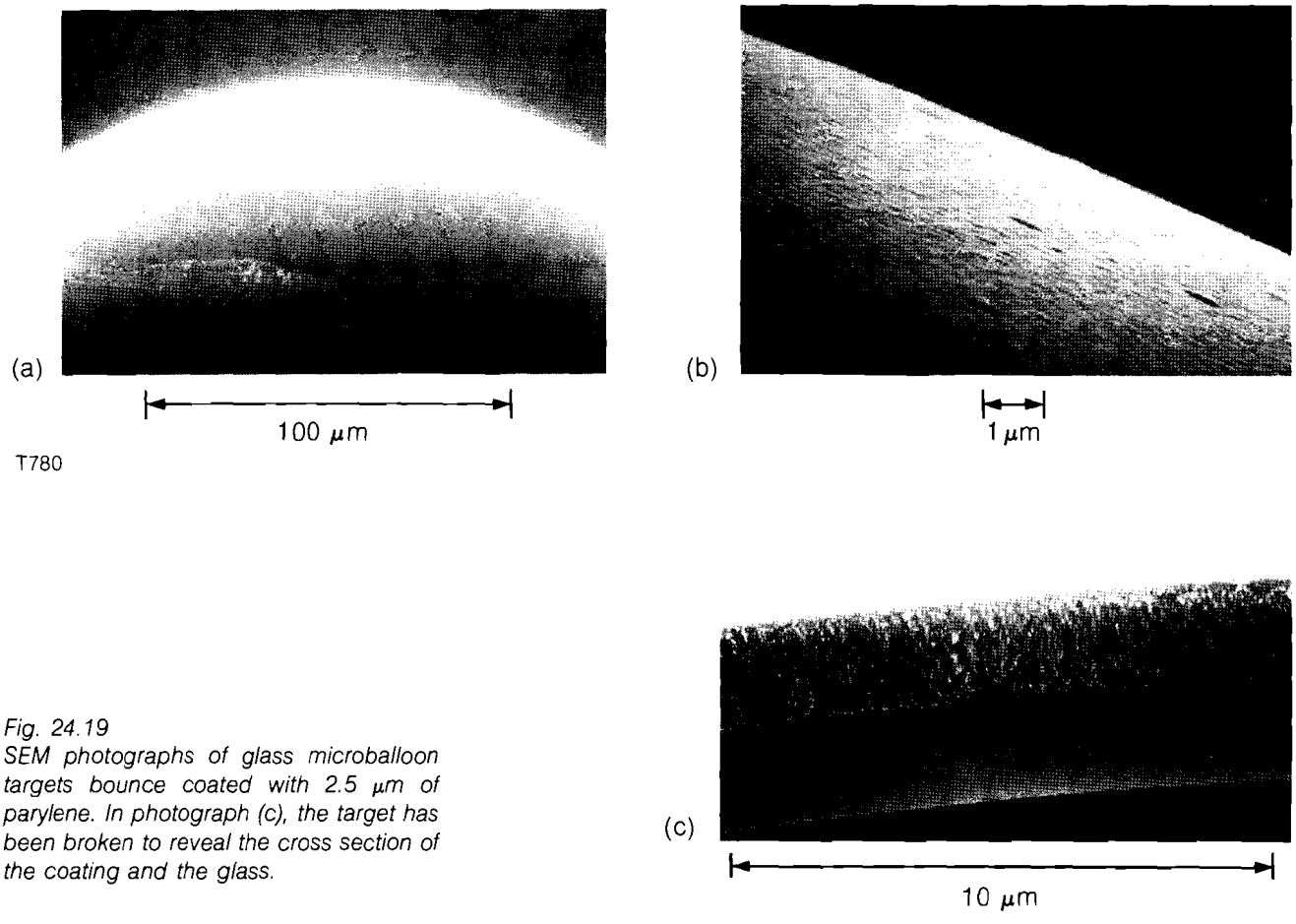

Fig. 24.19
SEM photographs of glass microballoon targets bounce coated with 2.5 μm of parylene. In photograph (c), the target has been broken to reveal the cross section of the coating and the glass.

It is seen in Fig. 24.19 that the application of the low-power plasma does not degrade the quality of the coating. The interior of the film shown in the fractured cross section [Fig. 24.19(c)] is of solid density, devoid of pores. This is similar to what is obtained with conventional parylene coating.[12] The thickness of the coating can also be estimated from Figure 24.19(c). However, x-ray radiography offers a more accurate means of determining film thickness and uniformity. The fact that radiography is nondestructive is also an advantage over the SEM measurements. Figure 24.20 shows an x-ray radiograph of a bounce-coated target. The 6.3-μm film thickness measured from Fig. 24.20 agrees with the interferometric measurements[7] within the 7% measurement uncertainty. Figure 24.20 also shows the film to be uniform within the measurement uncertainty. These initial results indicate that the optical interferometer can accurately measure and monitor the coating thickness during the bounce-coating process.

In conclusion, we have developed a cylindrical resonator for bouncing inertial fusion targets and used it for coating targets with parylene ablation layers. Several vibrational modes of the cylinder are found to be useful: longitudinal modes for bouncing and flexural modes for unsticking the targets. The cylinder has kept targets bouncing during coating runs that last many hours, producing ablation layers of high quality.

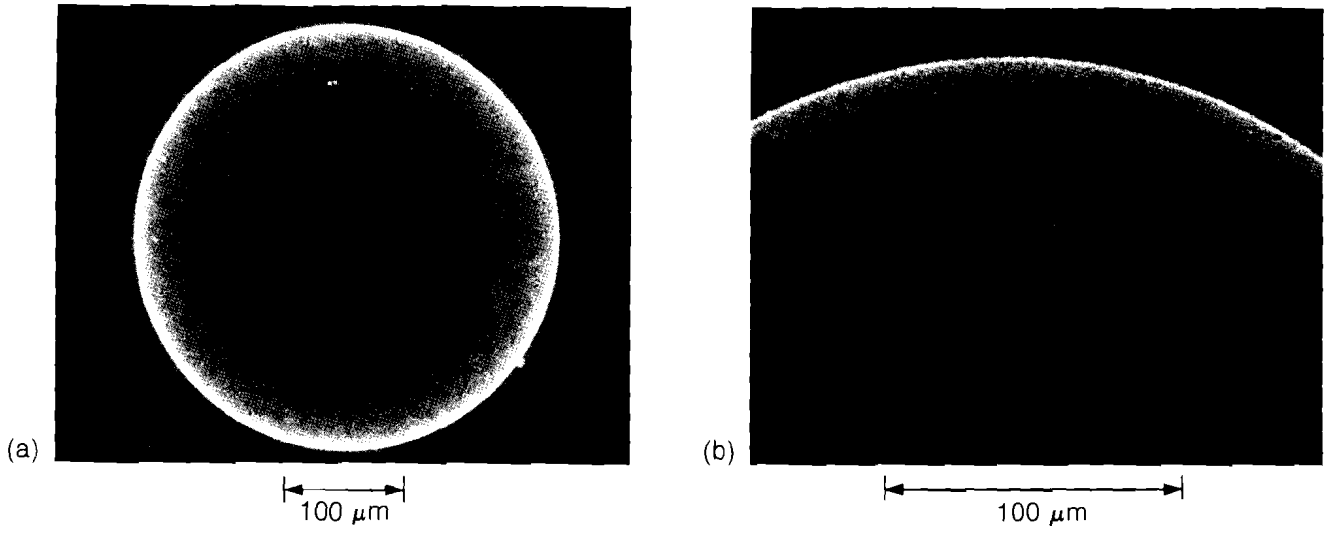

Fig. 24.20
X-ray radiographs of a target coated with 6.3 μm of parylene.

ACKNOWLEDGMENT

This work was supported by the U.S. Department of Energy Office of Inertial Fusion under agreement number DE-FC08-85DP40200 and by the Laser Fusion Feasibility Project at the Laboratory for Laser Energetics which has the following sponsors: Empire State Electric Energy Research Corporation, General Electric Company, New York State Energy Research and Development Authority, Northeast Utilities Service Company, Ontario Hydro, Southern California Edison Company, The Standard Oil Company, and University of Rochester. Such support does not imply endorsement of the content by any of the above parties.

REFERENCES

1. R. L. McCrory, L. Montierth, R. L. Morse, and C. P. Verdon, *Laser Interaction and Related Phenomena* (Plenum, New York, 1981), Vol. 5, pp. 713-742.
2. B. A. Brinker, J. M. Cavese, J. R. Miller, S. G. Noyes, S. Sheble, and L. T. Whitaker, *J. Vac. Sci. Technol. A* **1**, 941 (1983).
3. S. L. Letts, D. W. Meyers, and L. A. Witt, *J. Vac. Sci. Technol.* **19**, 758 (1981).
4. M. C. Lee, I. Feng, D. D. Elleman, T. G. Wang, and A. T. Young, *J. Vac. Sci. Technol.* **20** (1982).
5. R. Liepins, M. Campbell, J. S. Clements, J. Hammond, and R. J. Fries, *J. Vac. Sci. Technol.* **18**, 1218 (1981).
6. Union Carbide, parylene technology brochure.
7. H. Kim, T. Powers, and J. Mason, *J. Vac. Sci. Technol.* **21**, 900 (1982).
8. D. Bancroft, *Phys. Rev.* **59**, 588 (1941).
9. W. E. Tefft, *J. Res. Nat. Bur. Stand. (U.S.) B* **64B**, 237 (1960).
10. R. Q. Gram, D. H. Douglass, and J. A. Tyson, *Rev. Sci. Instrum.* **44**, 857 (1973).
11. S. Gracewski (private communication).
12. LLE Review **9**, 21 (1981).

3.B Liquid Crystal Soft Apertures

High-quality, laser-beam apodization has been the goal of solid-state laser device research programs since the early 1970s. The ability to shape the spatial intensity profile of a low- to moderate-power laser beam, prior to propagation through several stages of amplification, to a large extent determines the ultimate performance of high-peak-power and high-average-power systems.

The effect of a perfect apodizer device is illustrated schematically in Fig. 24.21. With this element one can create a quasi-flat-topped intensity profile from a Gaussian input. The soft edges of the apodizer minimize the occurrence of Fresnel diffraction rings in the output beam, permitting its propagation and amplification with a large fill factor and minimal small-scale self-focusing.

A perfect apodizer preserves the temporal shape of the input pulse and causes little distortion to the phase across the transmitted beam profile. Transmission in the device clear aperture is close to 1.0, whereas transmission at the edge falls to less than 10^{-3}. Good circular symmetry of the apodizer is a requirement for most applications, as is an edge profile that approximates the transmittance function

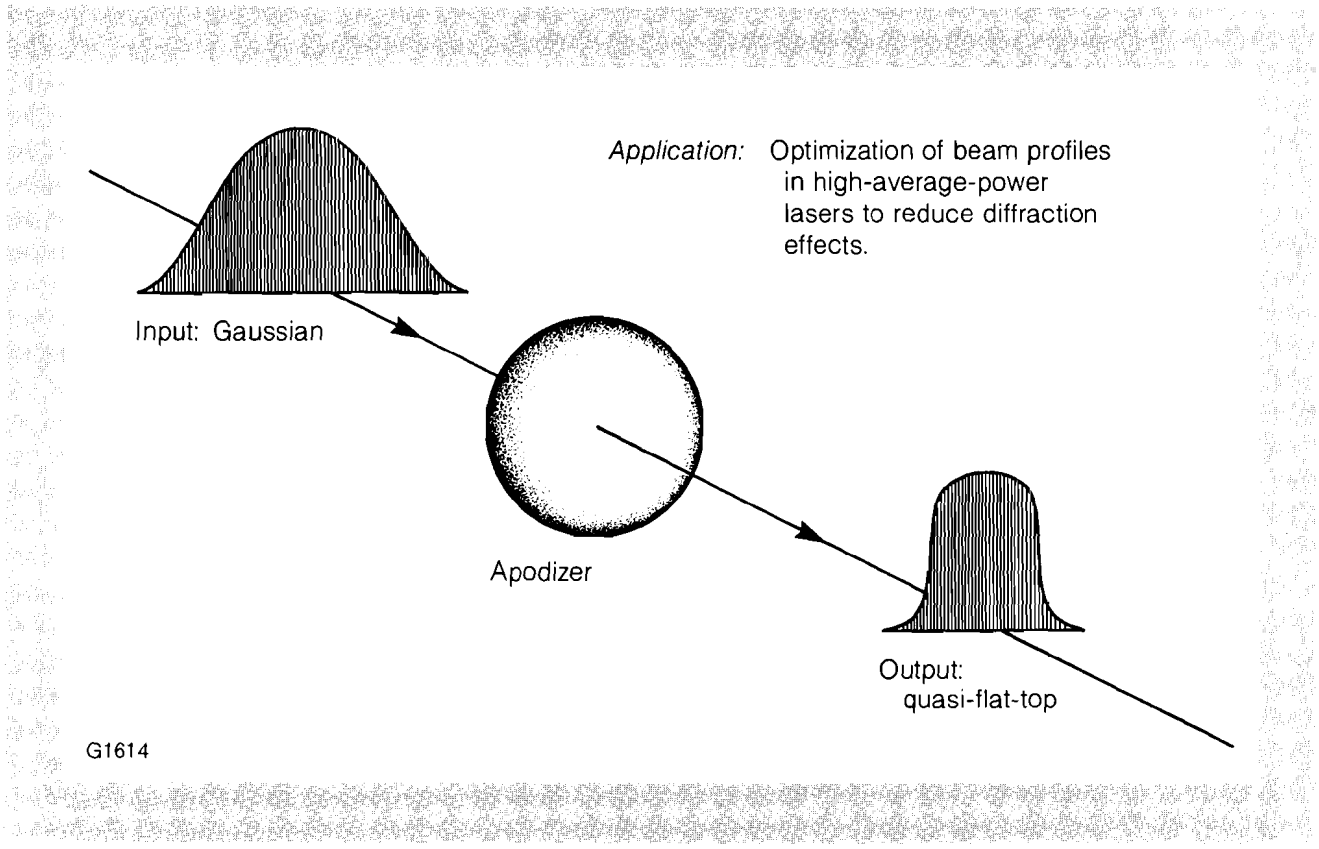

Fig. 24.21
Laser beam apodizer. A perfect apodizer truncates the wings of a Gaussian input without introducing diffraction effects. Good optical phase quality and intensity in the center of the beam are preserved.

$$I(r) = I_o \exp[-(r/r_o)^N], \; N = 5 \text{ to } 10, \qquad (1)$$

where the radial clear aperture parameter r_o is selected on the condition that $I(r_1) = 10^{-3} I_o$, where $2r_1$ is the entry aperture of the amplifying device that follows the apodizer.[1] Finally, the device must exhibit a high degree of laser damage resistance for high-peak-power applications, and low absorptive losses for high-average-power applications.

The fact that no perfect apodizer has been created is evident from the literature. The following passive-device technologies have been pursued:

(1) shaped absorbing liquid cells[2]
(2) saturable absorbers[3]
(3) shaped solid absorbers[2,4,5,6]
(4) graded photographic emulsion[2,7,8]
(5) graded metallic films[2,9]
(6) single and multilayer dielectric films[2]
(7) total internal reflection devices[1,2,10]
(8) radially birefringent elements[12–15]
(9) annular lens[16]

Electro-optic and magneto-optic concepts have also been proposed,[2] but none of these passive or active approaches has found broad acceptance. In fact, most high-peak-power solid-state laser systems, like LLE's OMEGA, use a hard aperture and an image-relaying scheme

invented by Hunt *et al.*[17] to maximize fill factor and minimize diffraction effects.

At LLE we have recently developed a new apodizer device based upon liquid crystal technology, which has demonstrated properties nearly like those of a perfect apodizer. Originating from our previous work with liquid crystal polarizers (LLE Review **21**, 8) and laser-blocking notch filters (LLE Review **15**, 30), our liquid crystal soft aperture possesses the following characteristics:

(1) passive and nonabsorptive, with no aperture limitations
(2) wavelength selectivity from UV to IR
(3) no input polarization requirements
(4) ease of fabrication in circular or other cross sections
(5) high laser-damage resistance
(6) low wave-front distortion

The concept of a liquid crystal soft aperture follows directly from the operating principles of a laser-blocking notch filter. Figure 24.22 illustrates the evolution of the device. In the conventional liquid crystal notch filter of Fig. 24.22(a), the LH and RH fluids act as a pair of crossed circular polarizers for incident laser radiation at wavelength λ_o. Light of any polarization state at that wavelength is reflected from the filter with a blocking efficiency approaching 10^4, provided (1) that the thickness of each fluid layer is at least 11 μm and (2) that the internal pitch of each fluid is equal in magnitude but opposite in chirality. The

Fig. 24.22
Evolution of the concept for liquid crystal soft aperture. By changing the shape of the central spacer element in a conventional laser-blocking notch filter, we can synthesize filters with radially varying transmission profiles. Blocking extinction, which originates from the selective reflection effect, varies from zero at element center to greater than 10^3 at the edge. Refractive index matching between the fluids and the glass minimizes phase distortion.

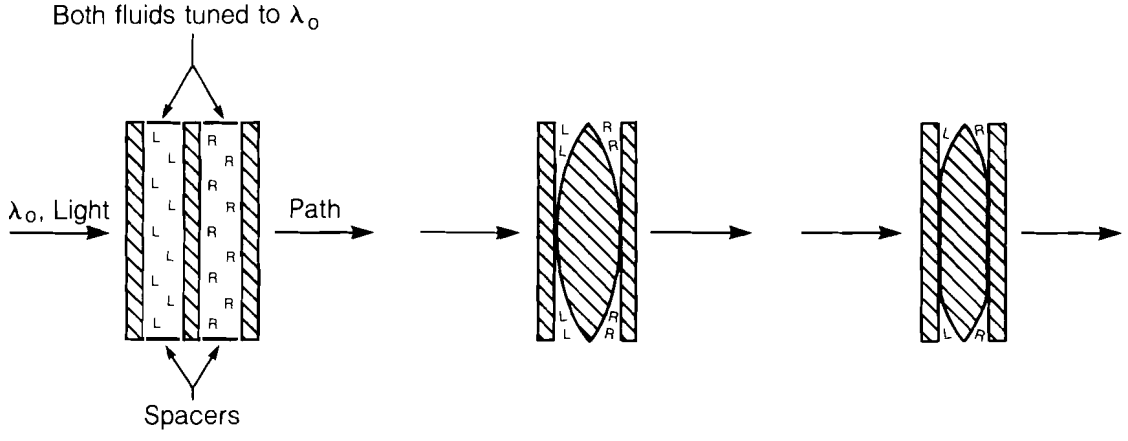

(a) Conventional Laser-Blocking Notch Filter

(b) Radial Notch Filter

(c) Radial Notch with Flattened Center

G1616

selective reflection effect can be made radially varying if curved surfaces are employed on the central spacer glass, as shown in Fig. 24.22(b). The fluid path is therefore made negligible at the center of the filter and increases to tens of micrometers at the filter edge. Blocking extinction increases radially with fluid layer thickness.

The cell geometry most useful for apodizer devices is illustrated in Fig. 24.22(c). Here, a biconvex central element has had optical flats polished onto the center of each curved surface. The flats determine the clear aperture of the apodizer, and the soft edge is created by the increase in LH and RH fluid layer thickness along the device radius. Fundamental to the success of the configuration shown in Fig. 24.22(c) is the ability to adjust the average refractive index of each liquid crystal layer to match that of the confining substrates to one part in 10^3 to 10^4. This minimizes optical wave-front distortion across the device clear aperture and well into the soft edge. The reflective nature of the effect promotes a high laser-damage resistance and minimal thermally induced distortions at high average powers.

We have designed liquid crystal soft apertures for use at $\lambda = 1064$ nm. The transmission profile of this type of apodizer at the soft edge is modeled by an equation of the form

$$I(r) = I_0 \, e^{-Qt(r)}, \tag{2}$$

where Q is a factor that describes the quality of liquid crystal alignment, and t(r) is the LH or RH fluid gap thickness in micrometers. For flattened, spherical central spacer elements, the functional form for t is given as

$$t(r, \text{microns}) = \frac{r^2 - r_0^2}{4f(n-1)} \times 10^3 \; (r \geq r_0), \tag{3}$$

where r_0 = radius of flattened clear aperture [as defined in Eq. (1)] in mm,
r = radial distance from the center of the device, in mm,
f = focal length of biconvex lens, in mm, and
n = refractive index of lens material, at λ_0.

Measurements on numerous notch filter cells have shown that Q varies depending upon the method and materials we choose to use in the preparation of our substrates. Figure 24.23 specifies those substrate surfaces that require a unidirectional rub with 1/10-μm diamond paste. (As previously described,[14,18] macroscopic alignment of liquid crystal molecules must be externally induced by the creation of microgrooves.) Because we have only recently begun to work with curved surfaces, we have experienced some variability in alignment results on the central spacer element of our soft apertures. Figure 24.24 shows the degree of blocking extinction as a function of fluid gap thickness for a *well-aligned*, wedged notch filter. Equation (2) fits the experimental data with a Q factor of 0.34.

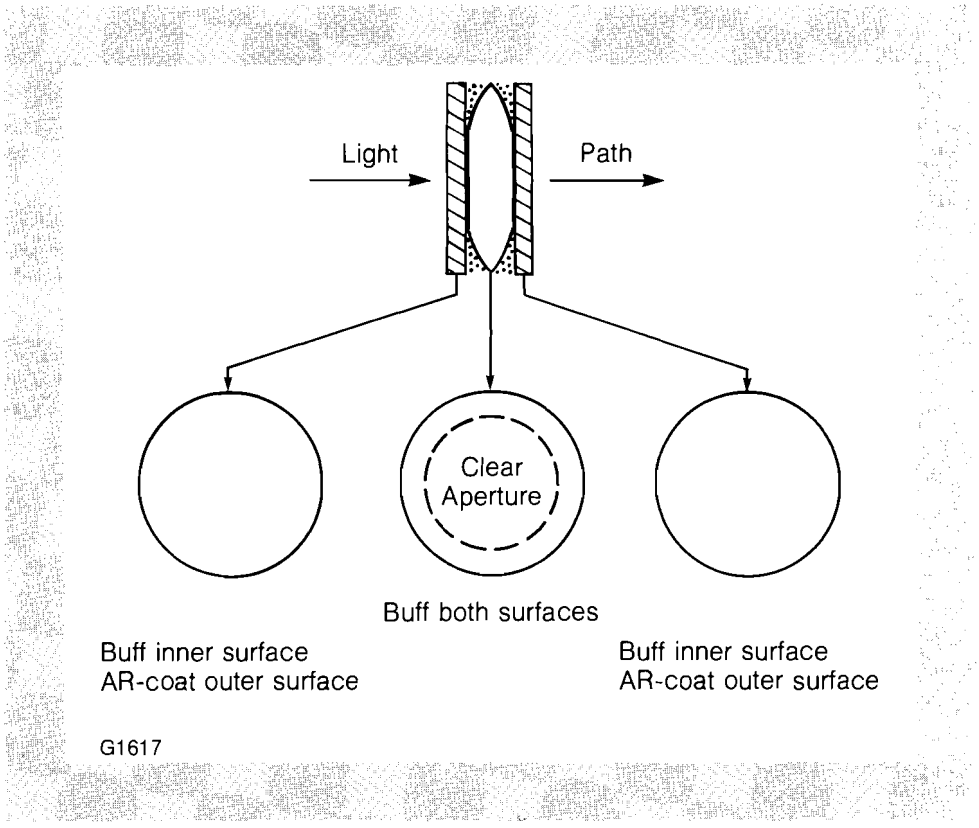

Fig. 24.23
Liquid crystal soft aperture construction. Unidirectional rubbing of substrate inner surfaces is required prior to cell assembly. This promotes macroscopic alignment of the liquid crystal molecules over apertures of several cm.

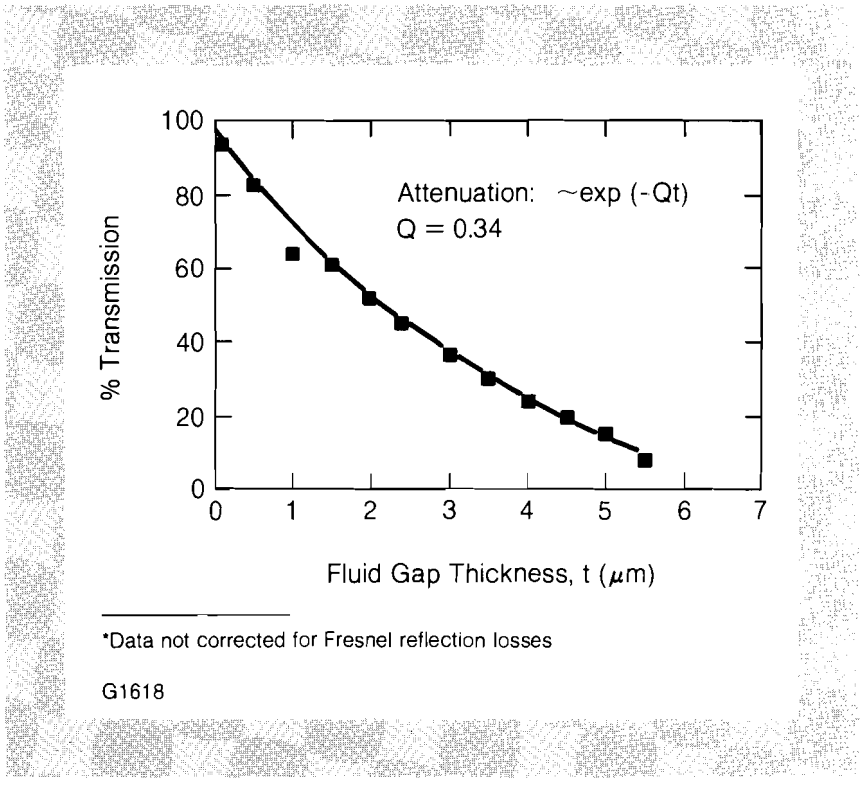

Fig. 24.24
Notch filter transmittance as a function of fluid gap thickness at λ = 1064 nm. This data is required to estimate the thickness dependence of the blocking extinction in the edge region of the liquid crystal soft aperture.

We have fabricated and constructed several prototype soft apertures, based on the design considerations described above. The dimensions and transmission profile of a 1064-nm soft aperture are given in Fig. 24.25. The profile was generated by scanning across the apodizer with a linearly polarized Nd:YAG laser beam whose focused beam waist was 150 μm $\pm$10% in dimension ($1/e^2$). (The noise in the profile is due to instabilities in the scanning laser and is not a result of any defects in the apodizer.) Interferometry at 1064 nm, also performed on this soft aperture, was used to determine the amount of wave-front distortion in the area of the soft edge. The transmission profile is replotted in Fig. 24.26 against the wave-front distortion. Figure 24.26 demonstrates that, with index matching to one part in 10^3 and temperature control to $\pm 2°C$ (the temperature coefficient of the refractive index for our fluids is approximately $-3 \times 10^{-4}/°C$), we can keep wave-front distortion below 0.25 waves at a point on the soft edge where transmittance drops to 20%. Glass apodizers exhibit a wave-front distortion in excess of 1.2 waves at their 20% transmittance point.

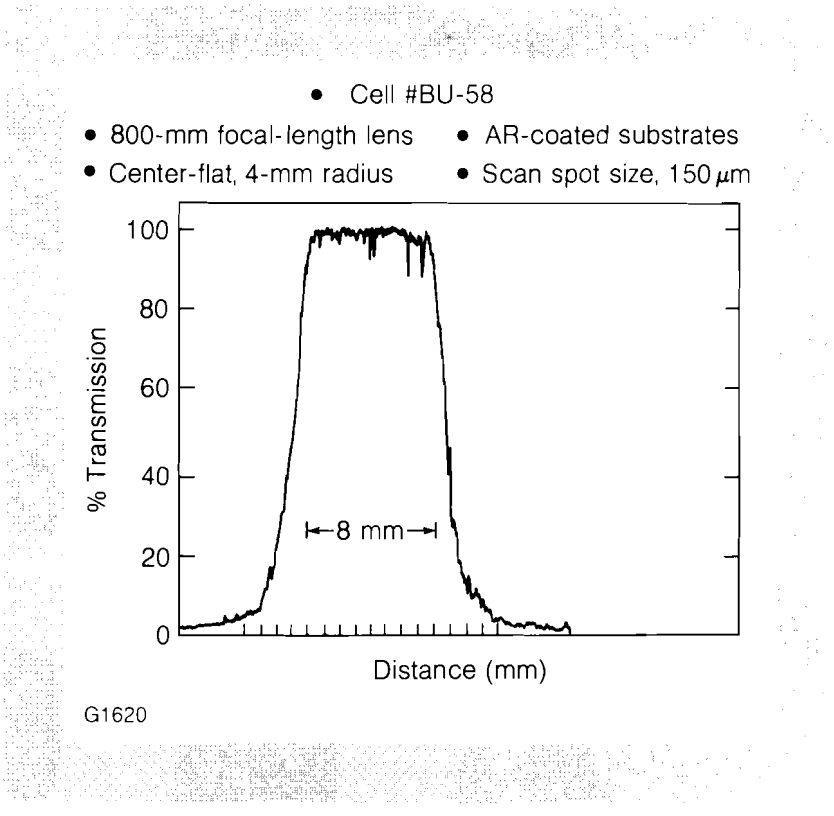

Fig. 24.25
Transmission profile scan for a liquid crystal soft aperture at λ = 1064 nm.

The calculated transmittance profile, using Eqs. (2) and (3) and the appropriate constants (f = 800 mm, r_o = 4 mm, n = 1.50), fits the measured one in Fig. 24.26 if a Q factor of 0.17 is assumed. This suggests that the quality of alignment is adequate, but not optimal. Improved alignment would steepen the profile to that depicted by the dotted line in Fig. 24.26. This would further improve the wave-front quality of the device.

Liquid crystal soft apertures have been made and delivered to experimentalists outside of LLE for testing and evaluation. The high laser

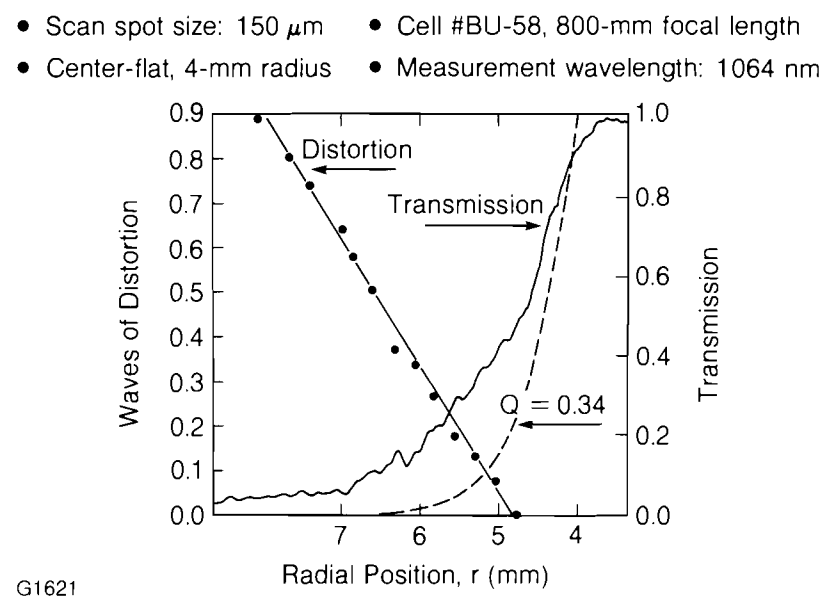

Fig. 24.26
Phase distortion in the edge region of a liquid crystal soft aperture. An enlargement of the transmission scan from Fig. 24.25 is superimposed upon phase distortion measurements made with interferometry at 1064 nm. Wave-front distortion less than λ/4 is maintained out to the point where transmission drops to 20%. Improvements in the quality of liquid crystal alignment (see dashed curve) will reduce wave-front distortion to less than λ/10.

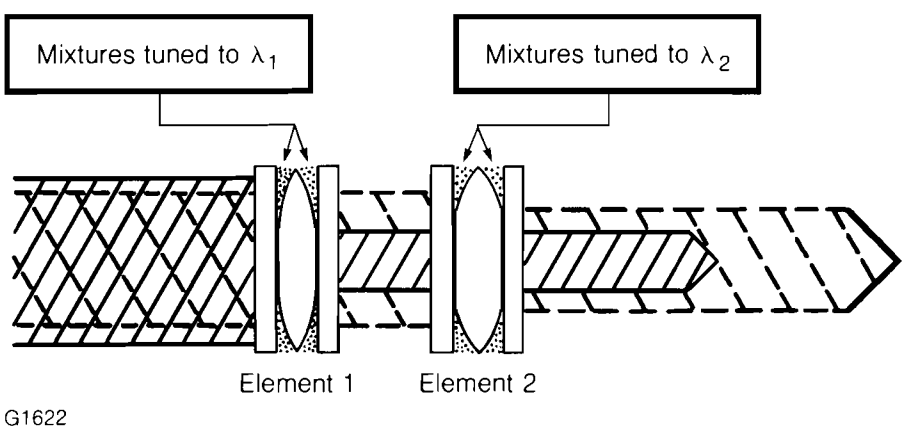

Fig. 24.27
Liquid crystal soft aperture flexibility. Because the selective reflection effect in liquid crystals is wavelength specific, liquid crystal soft aperatures may be stacked in tandem to operate on collinearly propagating laser beams whose wavelengths differ. Light at a given laser wavelength may be apodized with a unique clear aperture size and soft edge profile without affecting light at other wavelengths. No other technology exists that can perform in a similar fashion.

damage resistance[18] and low absorption of the liquid crystal compounds used to construct this device should permit its use in high-peak and high-average-power systems operating in the UV to near IR. The wavelength selectivity of the selective reflection effect permits apodization of one wavelength only, in situations where two or more wavelengths propagate collinearly (see Fig. 24.27). No other technology exists that can perform in a similar fashion.

ACKNOWLEDGMENT

This work was supported by contracts with the Advanced Laser Technology Group at General Electric Company, Binghamton, NY.

REFERENCES

1. I. K. Krasyuk *et al.*, *Sov. J. Quantum Electron.* **6**, 725 (1976).
2. V. R. Costich and B. C. Johnson, *Laser Focus*, 43, (September 1974).
3. A. Penzkofer and W. Frölich, *Opt. Commun.* **28**, 197 (1979).
4. Y. Asahara and T. Izumitani, U.S. Patent No. 4108621 (22 August 1978).
5. G. Dubé, *Advanced Laser Technology and Applications* (SPIE, Bellingham, WA, 1982), Vol. 335, p.10.
6. V. I. Kryzhanovskii, *Sov. J. Quantum Electron.* **13**, 194 (1983).
7. A. J. Campillo, B. Carpenter, B. E. Newnam, and S. L. Shapiro, *Opt. Commun.* **10**, 313 (1974).
8. E. W. S. Hee, *Optics and Laser Technology*, 75 (April 1975).
9. S. B. Arifzhanov *et al., Sov. J. Quantum Electron.* **11**, 745 (1981).
10. G. Dubé, *Opt. Commun.* **12**, 344 (1974).
11. J. C. Diels, *Appl. Opt.* **14**, 2810 (1975).
12. S. B. Papernyi, V. A. Serebryakov, and V. E. Yashin, *Sov. J. Quantum Electron.* **8**, 1165 (1978).
13. G. Giuliani, Y. K. Park, and R. L. Byer, *Opt. Lett.* **5**, 491 (1980).
14. S. D. Jacobs, *Polarizers and Applications* (SPIE, Bellingham, WA, 1981), Vol. 307, p.98.
15. J. M. Eggleston, G. Giuliani, and R. L. Byer, *J. Opt. Soc. Am.* **71**, 1264 (1981).
16. B. J. Feldman and S. J. Gitomer, *Appl. Opt.* **16**, 1484 (1977).
17. J. T. Hunt, J. A. Glaze, W. W. Simmons, and P. A. Renard, *Appl. Opt.* **17**, 2053 (1978).
18. S. D. Jacobs, K. A. Cerqua, T. J. Kessler, W. Seka, and R. Bahr, LLE Report No. 163, to be published as *NBS Special Publication: 16th Annual Symposium on Optical Materials for High-Power Lasers, Boulder, CO, October 1984.*

Section 4
PICOSECOND RESEARCH

4.A Genesis of Melting

The fundamental process responsible for initiating the melting of condensed matter has remained a mysterious and as yet unsolved problem. The longstanding interest in this most basic of phase transitions has nevertheless resulted in a great number of theoretical interpretations. The key question still to be answered is: What happens on the atomic scale when a crystal melts?

The only theory that deals with an actual microscopic mechanism capable of initiating a melt is the Defect Theory of Melting.[1] This model describes the formation of the liquid phase from the generation of defects: vacancies,[2] interstitials,[3] or dislocations.[4] The theory happens to be also consistent with the Lindemann Criterion, which is the only generally valid observation that defines at what stage melting occurs. However, as with all theories on melting, there has not been any experimental verification because of the difficulty in making a microscopic observation on a time scale appropriate to the ongoing process.

In the past ten years the short-pulse laser has evolved as an ideal tool for studying phase transitions. In addition to supplying energy densities large enough to create a melt in a time much shorter than the transition time, the optical pulse can also be used to probe the melting substance. An important consequence of this feature is that we can now drive a solid to a super-heated temperature faster than the system can respond. Figure 24.28 shows a conventional phase

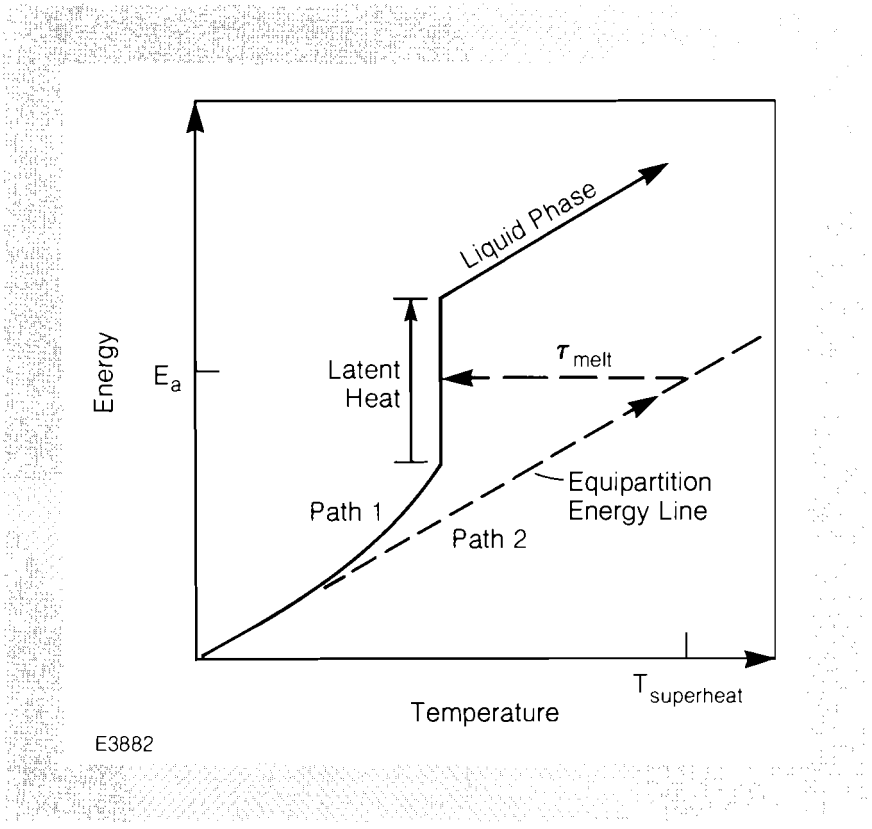

Fig. 24.28
Caloric diagram of the solid and liquid phases for a simple metal. Path 1 is followed when the energy is deposited on a time scale slower than the defect formation time. Path 2 is followed when the energy is deposited instantaneously.

diagram where Path 1 is followed under normal equilibrium conditions. If a quantity of energy E_a is rapidly deposited into the system, the path taken is along the equipartition energy line (Path 2). Depending on the peak power of the laser pulse and the system in question, the range over which superheating occurs is several thousand degrees. The time τ_{melt} is then the actual material-dependent melting time. The departure of Path 1 from the equipartition line is indicative of defect formation. With the short-pulse laser and a suitable probe, the rate of defect formation even below the melt threshold can be time resolved.

Several probe techniques have now been developed to time resolve phase transformations in semiconductors during laser annealing. However, most of these probes (e.g., electrical conductivity,[5,6] optical reflection,[7,8] optical transmission,[9] Raman scattering,[10] and time-of-flight mass spectrometry[11]) supply no direct information about the atomic structure or the temperature of the material. Probing the structure can reveal when and to what degree a system melts as it is defined by degradation in the long-range order of the lattice. True structural probes based on x-ray[12] and low-energy electron diffraction,[13] and EXAFS[14] with nanosecond time resolution, have been developed offering fresh insight into both the bulk and surface dynamics of material structure. Also, a subpicosecond probe based on structurally dependent second-harmonic generation[15] has been demonstrated. But at present, only the technique of picosecond electron diffraction[16] can produce an unambiguous picture of the atomic structure on the picosecond time scale.

In this article we describe an experiment utilizing this instrument to time resolve the laser-induced phase transition in aluminum. The results are then interpreted in the context of the defect theory of melting.

Experiment and Results

The technique takes advantage of the strong scattering efficiency of 25-keV electrons in transmission mode to produce and record a diffraction pattern with as few as 10^4 electrons in a pulse of 20-ps duration. The burst of electrons is generated from a modified streak camera that, via the photoelectric effect, converts an optical pulse to an electron pulse of equal duration.[17] Also of importance is that the electron pulse can be synchronized with picosecond resolution to the laser pulse.[18] The experimental arrangement is illustrated in Fig. 24.29. A single pulse from an active-passive mode-locked Nd^{+3}:YAG laser is spatially filtered and amplified to yield energies up to 10 mJ. The streak tube (deflection plates removed), specimen, and phosphor screen are placed in vacuum at 10^{-6}-mm Hg. The electron tube is comprised of the photocathode, extraction grid, focusing cone, and

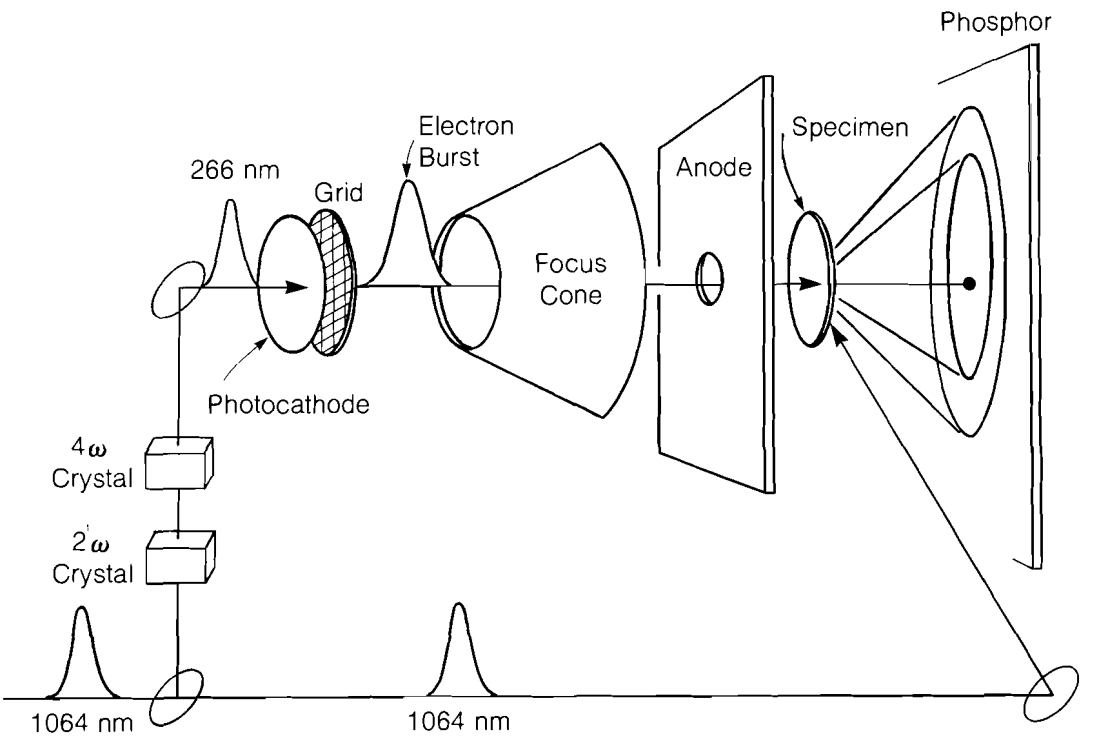

Fig. 24.29
Schematic of picosecond electron diffraction apparatus. A streak camera tube (deflection plates removed) is used to produce the electron pulse. The 25-keV electron pulse passes through the Al specimen and produces a diffraction pattern of the structure with a 20-ps exposure.

anode. A gold photocathode is used to permit the vacuum chamber to be opened to air. The photocathode is held at the maximum voltage (−25 kV) so that space charge, which can cause significant temporal broadening, is minimized. The portion of the laser irradiating the photocathode is first up-converted to the fourth harmonic of the fundamental wavelength in order to produce the electrons efficiently. The duration of the UV pulse, and thus the electron pulse, is ~ 20 ps. Once the electron pulse is generated it accelerates through the tube past the anode and then remains at a constant velocity. The specimen is located in this drift region. The electrons pass through the specimen with a beam diameter of 500 μm and come to a 200-μm focus at their diffracted positions on the phosphor screen. A gated-microchannel-plate image intensifier in contact with the phosphor screen amplifies the electron signal $\sim 10^4$ times.

A metal was chosen over a semiconductor as the specimen because of the ease with which metals can be fabricated in ultra-thin polycrystalline films. The specimens were fabricated by first depositing Al onto formvar substrates and then vapor-dissolving away the formvar. Freestanding films 250 ± 20 Å in thickness were required so that the electrons sustain, on the average, one elastic collision while passing through the specimen. This thickness of Al corresponds to twice the 1/e penetration depth at 1060 nm. It is worth noting that the penetration depth for a metal does not vary significantly from solid to liquid, as is the case with a semiconductor where a change in absorption of one to two orders of magnitude is possible. Since the diffusion length $(D\tau)^{1/2}$—where D is the thermal diffusivity coefficient (0.86 cm^2/s) and τ is time—is limited to 250 Å, the temperature in the Al is uniformly established in less than 10 ps. The absorption of the laser by aluminum is 13 ± 1%.

The diameter of the laser stimulus is ~ 4 mm ($1/e^2$) and is centered over the 2-mm specimen. A 1-mm pinhole, positioned in place of the specimen, facilitates accurate alignment of the laser beam profile to the electron beam. Using a 1-mm pinhole assures accurate measurement of the fluence within the probed region. Synchronization between the electron pulse and the laser stimulus is then accomplished by means of a laser-activated deflection plate assembly.[19]

The experimental procedure is then to stimulate the aluminum sample with the laser while monitoring the lattice structure at a given delay. The films are used only once, even though for low fluence levels ($\lesssim$ 8 mJ/cm^2) the films could survive repeated shots. Figure 24.30 shows the laser-induced time-resolved phase transformation of aluminum at a constant fluence of ~13 mJ/cm^2. The abrupt disappearance of rings in the diffraction pattern occurs with a delay of 20 ps. As is evident, the breakdown of lattice order can be induced in a time shorter than the resolution of our probe. However, the fluence required for this rapid transition exceeds F_{melt}, the calculated fluence required to completely melt the Al specimen under equilibrium conditions (~ 5 mJ/cm^2). At a constant fluence of 11 mJ/cm^2 the phase transition was again observed, but only after a probe delay of 60 ps. Figure 24.31 shows the melt metamorphosis of Al, where the points represent the

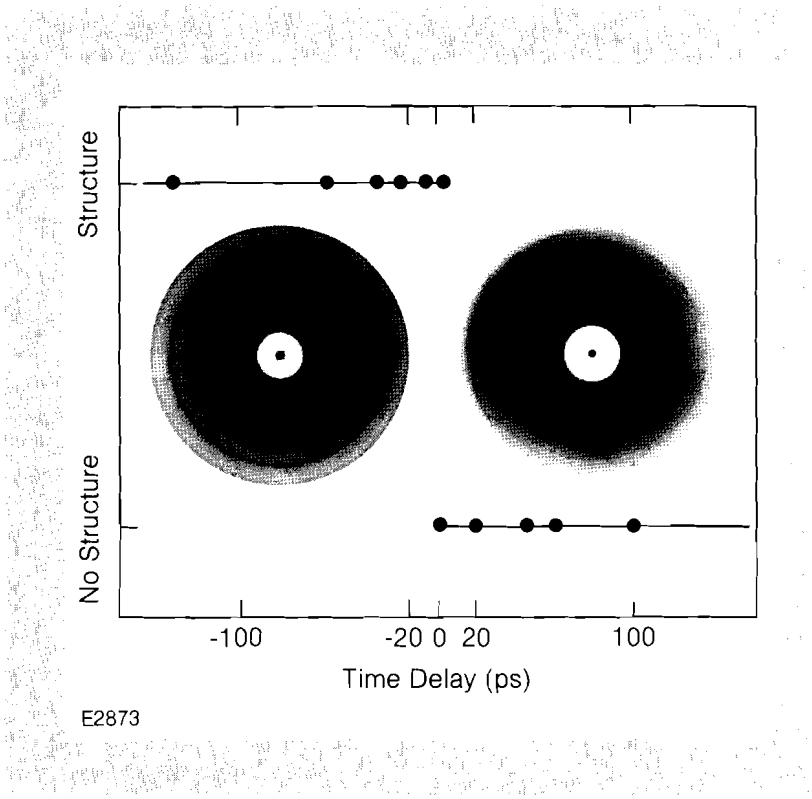

Fig. 24.30
Time-resolved laser-induced phase transition in aluminum. The pattern on the left is the diffraction pattern for Al and represents the points along the top line—where the electron pulse arrives before the laser stimulus. The pattern on the right shows the loss of structure in the Al 20 ps (or more) after applying the laser stimulus at a fluence of 13 mJ/cm^2. The fine line background structure occurring in both pictures is an artifact of the circular averaging technique.

delay time before the complete phase transition is observed for various fluence levels. We see that the elapsed time increases exponentially with decreased fluence, and at 7 mJ/cm^2 the delay is ~ 1 ns. Because the fluence level that is applied is always in excess of F_{melt}, the observed delay time suggests that the Al is first driven to a superheated solid state before melting. It must be pointed out that as the fluence was decreased the abruptness with which the rings disappeared became less dramatic. Consequently, determination of the precise delay increases in difficulty with decreasing fluence. The temperature scale represents the temperature of the superheated Al, assuming a linear increase in the specific heat with temperature. We see that temperatures in excess of 2000°K are expected, with fluence levels near 13 mJ/cm^2. The region beneath the curve represents the conditions under which the Al can be observed in a superheated solid state.

Interpretation

Let us assume that the disorder is induced by the generation of either vacancies or interstitials. The jumping frequency is then given by

$$\upsilon_J = \upsilon \exp\left(-\frac{E}{kT}\right),$$

where υ is the atomic vibrational frequency and E is the activation energy (1 eV for Schottky type, ~ 4 eV for Frenkel type, and 1 eV for self-diffusion).

If we further assume that a fixed number of vacancies is required to initiate the melt, we can then find the activation energy E from the slope

of the curve in Fig. 24.31

$$E = K \frac{\partial(\ell n\ \tau_{ob})}{\partial(1/T)} = 1 \pm 0.2 \text{ eV},$$

where T is temperature and τ_{ob} is the corresponding decay time for the melting process to be completed.

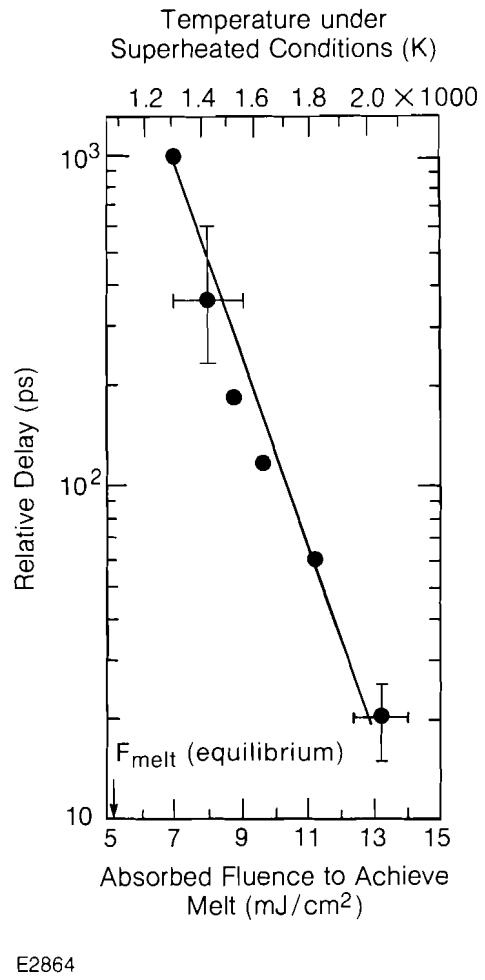

Fig. 24.31
Laser-induced melt metamorphosis for aluminum. The points mark the elapsed time for the diffraction rings to completely disappear. The vertical error bar represents the degree of uncertainty in defining the moment of complete melt. The region beneath the curve represents the conditions under which the Al is left in a superheated solid state.

The activation energy agrees surprisingly well with the required energy for Schottky defect formation, which suggests that the melt actually begins at the outer surfaces of the individual crystallites and propagates inward through self-diffusion. Figure 24.32 depicts a possible ultrafast scenario that is founded on the defect theory of melting. Just after illumination, the lattice is uniformly hot; surface defects then begin to form, cooling the lattice. A temperature gradient, corresponding to the defect gradient, is thus established. The two gradients persist until the crystal is saturated with defects and is said to be homogeneously melted.

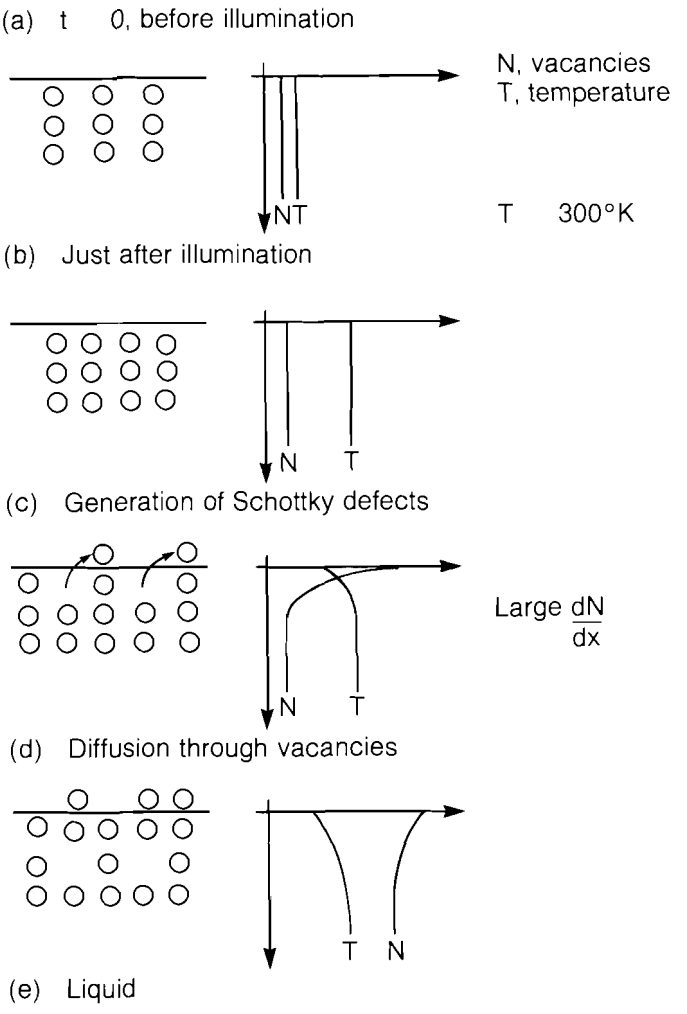

Fig. 24.32
Scenario for ultrafast melting based on the Defect Theory of Melting.

In conclusion, we have demonstrated that the picosecond electron-diffraction technique can be used to provide time resolution of the laser-induced melt evolution in aluminum. We found it possible to melt the aluminum completely in a time shorter than 20 ps if sufficient laser fluence is applied ($\gtrsim 2.6 \times F_{melt}$). The time required to melt the aluminum increases exponentially with decreasing fluence; at $1.4 \times F_{melt}$, the phase transition time increased to ~1 ns. During this time, the two phases coexist as a heterogeneous melt while the superheated solid is being continuously transformed into liquid. We have interpreted the results in terms of the defect theory of melting and found that the activation energy measured agrees with that of Schottky defect formation.

ACKNOWLEDGMENT

This work was supported by the following sponsors of the Laser Fusion Feasibility Project at the Laboratory for Laser Energetics—Empire State Electric Energy Research Corporation, General Electric Company, New York State Energy Research and Development Authority, Northeast Utilities Service Company, Ontario Hydro, Sourthern California Edison Company, The Standard Oil Company, and University of Rochester. Such support does not imply endorsement of the content by any of the above parties.

The authors would like to acknowledge the support of Jerry Drumheller, who assisted in the fabrication of the aluminum films, as well as to thank Hsiu-Cheng Chen for her help during the experiment.

REFERENCES

1. F. C. Frank, *Proc. R. Soc. London, Ser. A* **170**, 182 (1939).
2. J. Frenkel, *Kinetic Theory of Liquids* (Dover Publications, 1955).
3. J. E. Lennard-Jones and A. F. Devonshire, *Proc. R. Soc. London, Ser. A* **169**, 317 (1939); **170**, 464 (1939).
4. D. Kuhlmann-Wildorf, *Phys. Rev. A* **140**, 1599 (1965).
5. M. Yamada *et al., J. Phys. Soc. Jpn.* **49**, 1299 (1980).
6. G. J. Galvin *et al., Phys. Rev. Lett.* **48**, 33 (1982).
7. D. H. Auston *et al. Appl. Phys. Lett.* **33**, 437 (1978).
8. C. V. Shank, R. Yen, and C. Hirlimann, *Phys. Rev. Lett.* **50**, 454 (1983).
9. J. M. Liu, H. Kurz, and N. Bloembergen, *Appl. Phys. Lett.* **41**, 643 (1982).
10. H. W. Lo and A. Compaan, *Phys. Rev. Lett.* **44**, 1604 (1980).
11. A. Pospieszczyk, M. A. Harith, and B. Stritzker, *J. Appl. Phys.* **54**, 3176 (1983).
12. B. C. Larson, C. W. White, T. S. Noggle, and D. Mills, *Phys. Rev. Lett.* **48**, 337 (1982).
13. R. S. Becker, G. S. Higashi, and J. A. Golovchenko, *Phys. Rev. Lett.* **52**, 307 (1984).
14. H. M. Epstein, R. E. Schwerzel, P. J. Mallozzi, and B. E. Campbell, *J. Am. Chem. Soc.* **105**, 1466 (1983).
15. C. V. Shank, R. Yen, and C. Hirliman, *Phys. Rev. Lett.* **51**, 900 (1983).
16. G. Mourou and S. Williamson, *Appl. Phys. Lett.* **41**, 44 (1982).
17. D. J. Bradley and W. Sibbett, *Appl. Phys. Lett.* **27**, 382 (1975).
18. G. Mourou and W. Knox, *Appl. Phys. Lett.* **36**, 623 (1980).
19. S. Williamson, G. Mourou, and S. Letzring, *High Speed Photography*, (SPIE, Bellingham, WA, 1983), Vol. 348(I), p.197.

4.B Picosecond Electro-Electron Optic Oscilloscope

The technique of electro-optic sampling[1-3] presently offers the only means by which an electrical waveform can be time resolved with subpicosecond resolution. With a sensitivity of ~1 mV and the capability of sampling in a contactless configuration, this technique has become a valuable tool for the characterization of ultrafast electronic components. The contactless mode of sampling can also be scaled up to allow sampling on a plane surface, permitting the evaluation of any number of discrete components within an integrated circuit. In spite of these attractive features, the electro-optic sampling technique has been adopted by only a few large laboratories, the major drawback being the requirement of a short-pulse laser system. The complexity of such a laser results in a sampling oscilloscope that is delicate, maintenance intensive, and expensive, precluding its development in industry and many universities.

Recently, we have developed a conceptually new picosecond sampling oscilloscope that maintains the salient features of the electro-optic sampler while eliminating the need for a short-pulse laser. The new oscilloscope, called the electro-electron optic oscilloscope, represents the converse approach to electro-optic sampling.

Principle of Operation

In both systems the process of sensing an E-field-induced change in birefringence with polarized light is the same. What has changed (Fig. 24.33) is the replacement of the short-pulse laser with a cw laser and the slow-response detector with a streak camera. A streak camera is comprised of an electron image converting tube that, via the photoelectric effect, converts an optical pulse to an electron pulse replica. This electron pulse can then be rapidly deflected, or streaked in a time-varying electric field. An electron pulse streaked in this manner has its time axis mapped along the direction of deflection onto a phosphor screen, where it can then be recorded. With this arrangement, the temporal resolution of the oscilloscope is determined not by the shortness of an optical pulse, but by the resolution of the streak camera. Presently, streak cameras with a few picoseconds' resolution are commercially available. As depicted in Fig. 24.33, by using a cw laser each electrical signal is first converted to an optical replica, then to an electron replica within the streak camera. Consequently, each electrical waveform is sampled in its entirety with every shot.

Experiment And Results

The experimental setup is shown in Fig. 24.34. The modulator is a Lasermetrics Pockels cell having a response time of ~40 ps. The Pockels cell and Soleil compensator are placed between crossed polarizers. A 1-mw HeNe laser is used as the cw probe. The device being characterized is an HP step recovery diode model 33002-A that is driven at 85 MHz along with the deflection plates of the synchroscan-type streak camera. In this configuration, a simple phase shift between the two sine waves is all that is required for synchronizing the diode to the streak camera.

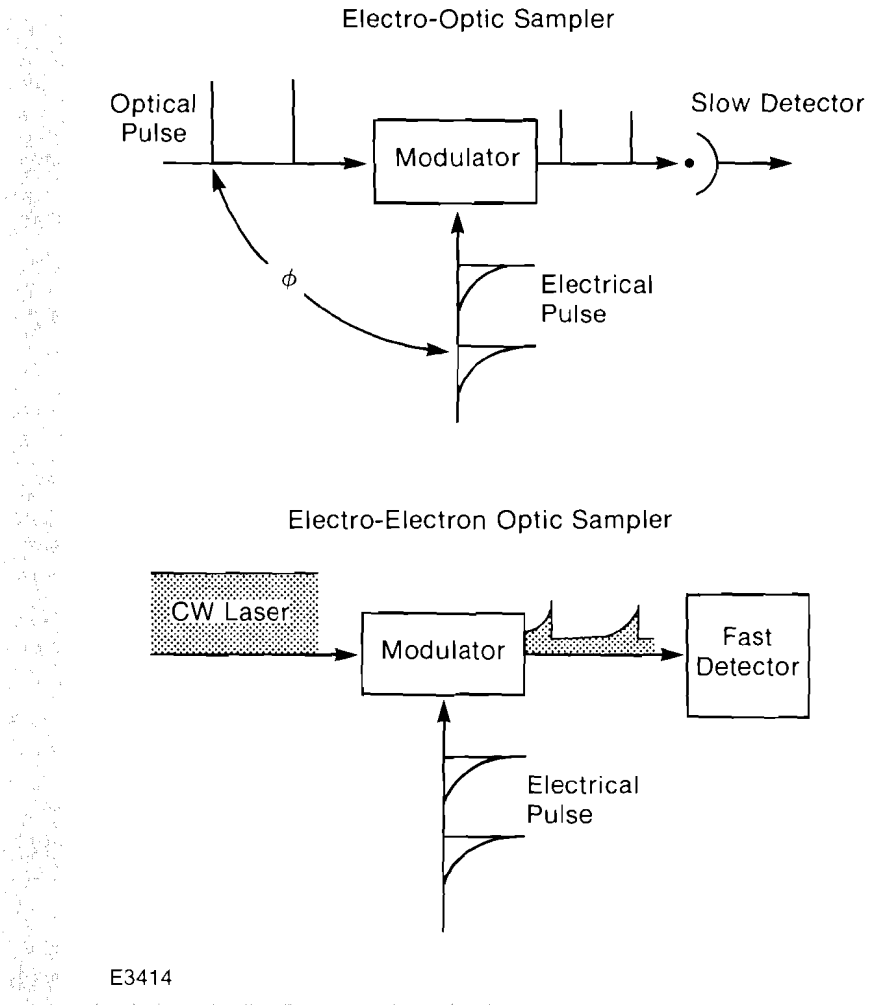

Fig. 24.33
Converse approaches to electro-optic sampling.

For the initial experiment, the compensator was adjusted to 50% transmission for maximum sensitivity of modulation, dT/dV. In order to operate at this point, it is necessary to attenuate the transmitted beam by five optical depths (OD). This assures us of an average current density from the photocathode safely below the damage threshold ($\sim$ 10 μA/cm^2). Attenuating the transmitted signal by 10^5, though, also attenuates the modulated signal by the same factor. As a consequence, no signal could be found even after several tens of seconds of integration time. However, we discovered that if we adjusted the optical compensator off the 50% transmission point down to a transmission factor of 10^{-5} and then removed the 5-OD optical attenuation, a signal large enough to be observed even in real time appeared on the streak camera monitor. An explanation for the enhancement of the modulated signal is offered from Figs. 24.35 and 24.36. In Fig. 24.35 we have

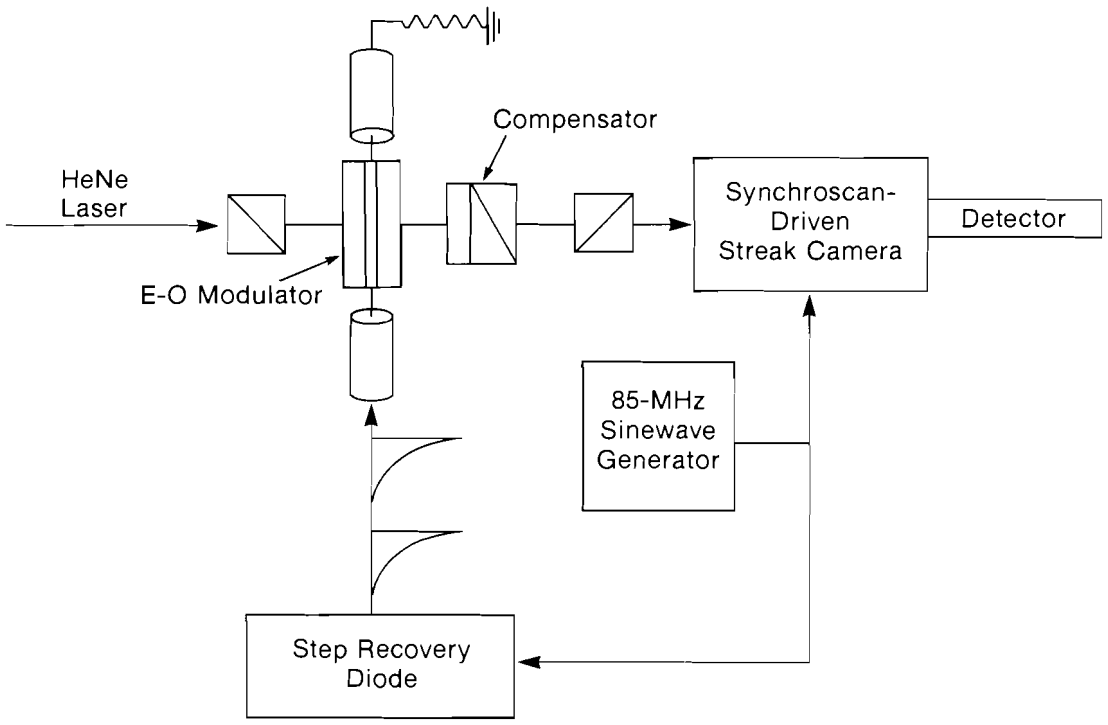

Fig. 24.34
Experimental layout.

plotted both the transmission function T for a modulator between crossed polarizers, as well as the corresponding sensitivity curve dT/dV. We see that the sensitivity indeed has its maximum at $V_\pi/2$, that is, at the 50% transmission point. However, when the transmitted background signal can only be a small portion of the incident signal, an enhancement in the depth of modulation *relative* to the background can nevertheless be achieved. By adjusting the compensator (or, equivalently, the dc bias voltage), the efficiency of modulation (dT/dV)/T goes as cot $[(\pi/2)\ V/V_\pi]$ (see Fig. 24.36). In this way, the number of modulated photons can be increased, in our case, by a factor of $\sqrt{10^5}$ over the conventional approach of biasing to 50% and then attenuating by 5 OD. Though each optical replica consists of just a few tens of photons, the synchroscan streak camera, upon accumulating 85×10^6 shots/s, reconstructs the waveform within seconds. It is important to bias slightly off the zero transmission point so that a signal possessing both polarities is not rectified. The issue of nonlinearity of response for the modulator is not a serious one since a maximum excursion of a few volts along a transmission curve whose V_π is 5000 V results in a deviation of less than 1% from a straight line. Figure 24.37 displays the signal of the step recovery diode. The response agrees well with a measurement made using a Tektronix sampling oscilloscope.

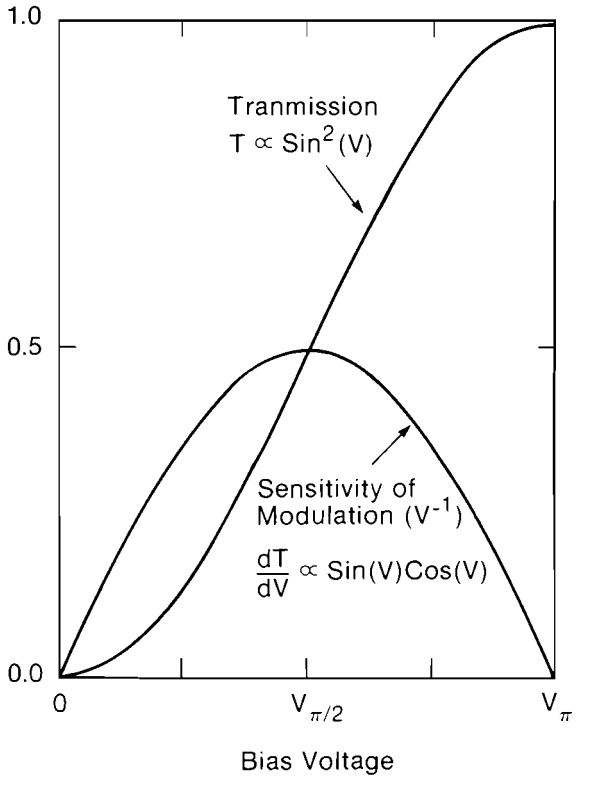

Fig. 24.35
Transmission and sensitivity of modulation curves for an electro-optic modulator.

In conclusion, we have developed a novel picosecond oscilloscope that is based on the electro-optic effect but eliminates the need for a short-pulse laser system. The electro-electron optic oscilloscope maintains the attractive features found in the electro-optic sampler but is relatively simple to operate, less expensive, and portable. In addition, the sampling frequency of this oscilloscope can be adjusted to accommodate the optimal operating frequency of the circuit in question. Any cw laser having a wavelength between 250 nm and 1000 nm can be chosen as the probe. As an example, a semiconductor laser can be used, allowing the probing of GaAs—which happens also to be an electro-optic material. Finally, because the electro-electron optic sampler samples each waveform in its entirety, the system can potentially be used in single-shot mode.

ACKNOWLEDGMENT

This work was supported by the following sponsors of the Laser Fusion Feasibility Project at the Laboratory for Laser Energetics—Empire State Electric Energy Research Corporation, General Electric Company, New York State Energy Research and Development Authority, Northeast Utilities Service Company, Ontario Hydro, Sourthern California Edison Company, The Standard Oil Company, and University of Rochester. Such support does not imply endorsement of the content by any of the above parties.

The authors would like to thank Norman Schiller and co-workers of the Hamamatsu Corp. for their willingness in offering both a streak camera and assistance, making the final result of this preliminary experiment possible.

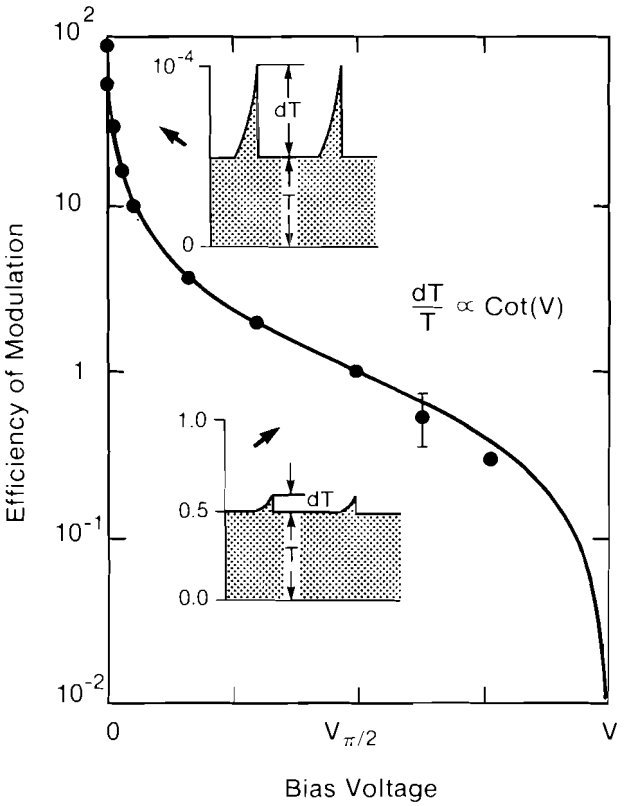

Fig. 24.36
Efficiency of modulation. Note difference in scales for the inserted transmission curves.

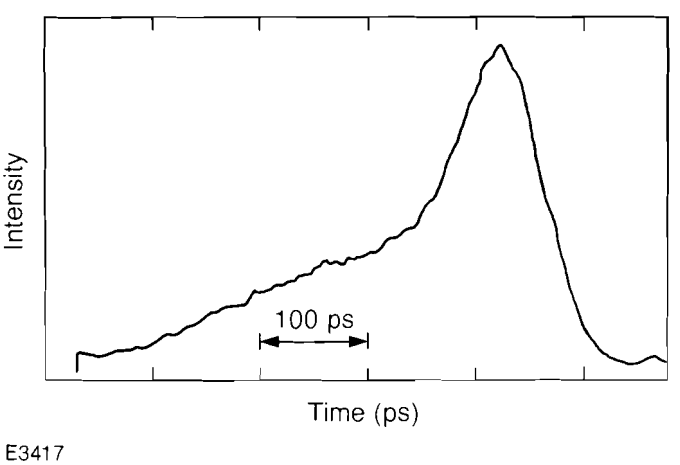

Fig. 24.37
Time-resolved response for step recovery diode.

REFERENCES

1. J. A. Valdmanis, G. A. Mourou, and C. W. Gabel, *Appl. Phys. Lett.* **41**, 211 (1982).

2. J. A. Valdmanis, G. A. Mourou, and C. W. Gabel, *IEEE J. Quantum Electron.* **QE-17**, 664 (1983).

3. G. A. Mourou and K. E. Meyer, *Appl. Phys. Lett.* **45**, 492 (1984).

Section 5
NATIONAL LASER USERS FACILITY NEWS

This report covers the activities of the National Laser Users Facility (NLUF) for the quarter 1 July to 30 September 1985. During this period five users conducted experiments on LLE facilities: one on GDL and four on OMEGA. In addition, the Department of Energy concurred with the steering committee recommendations.

For the user experiment on the GDL system, 527-nm light was focused onto thin-foil targets to study the Raman spectra and hot-electron emission spectra. (The GDL system was recently upgraded with active-mirror amplifiers to produce a doubler output of 250 J.) The participating individuals in this experiment were

- **Chan Joshi, Humberto Figueroa, Chris Clayton**, and **Ken Marsh** (University of California, Los Angeles): "Studies of the Two-Plasmon Decay and Stimulated-Raman-Scattering Instabilities in Long-Scale-Length Plasmas"

The user experiments on the OMEGA system were for a variety of applications, all utilizing the full 24 beams of 351-nm light focused onto spherical targets.

- **Burton L. Henke** and **Paul A. Jaanimagi** (University of Hawaii at Manoa): "Evaluation and Application of a Streak Camera and Photographic Camera Coupled Elliptical-Analyzer Spectrograph System for the Diagnostics of Laser-Produced X-Ray Sources (100–10,000-eV region)"

- **Hans R. Griem, Samuel Goldsmith**, and **Aaron Krumbein** (University of Maryland): "A Proposal for Thermal Transport Studies Using Extreme Ultraviolet Spectroscopy"
- **Carl B. Collins** and **Suhas S. Wagal** (University of Texas at Dallas): "Continuation of the Study of Nuclear Fluorescence Excited by Laser Plasma X Rays"
- **C. F. Hooper, Jr.** (University of Florida): "A Study of Plasma-Induced Continuum Lowering and Spectral Line Alterations: A Proposal to NLUF"
- **Allan Hauer, James Cobble, William Mead**, and **Phil Goldstone** (Los Alamos National Laboratory): "Diagnostics of High-Density Laser-Driven Compressions with Novel X-Ray Spectroscopic Techniques"

Additional information on these experiments can be obtained from the scientists associated with the experiment.

Also in this quarter, the Department of Energy informed us that they concur with the steering committee's technical recommendation for proposals reviewed at the meeting of 4 March 1985.

Ten of the proposals were approved for facility time. Individual funding levels for these experiments were recommended to DOE for their consideration. The committee noted the continued excellence of user experiments.

The new approved proposals are listed below in alphabetical order.

- **John Apruzese** (Naval Research Laboratory): "Demonstration of Gain in Neon-Like Tin Using Collisional Pumping by Suprathermal Electrons"
- **Carl B. Collins** (The University of Texas at Dallas): "Continuation of the Study of Nuclear Fluorescence Excited by Laser Plasma X Rays"
- **Dwight Duston** (Naval Research Laboratory): "Studies of Dielectronic Satellite Emission in Ultra-Dense Plasmas"
- **Uri Feldman** (Naval Research Laboratory): "A Proposal for Spectroscopic Studies Relevant to X-Ray Lasers Using the OMEGA Laser"
- **T. R. Fisher** (Lockheed Applied Physics Laboratory): "Measurement of the Time-Dependent Distribution of Ionization States in an Argon Plasma from a Mach-10 Jet"
- **Hans R. Griem** (University of Maryland): "Thermal Transport Studies Using Extreme Ultraviolet Spectroscopy"
- **Burton L. Henke** (Lawrence Berkeley Laboratory): "Continued Development, Evaluation, and Application of a Streak Camera/Photographic Camera Elliptical-Analyzer X-Ray Spectrograph System (SPEAXS) for the Diagnostics of Laser-Produced X-Ray Sources (100–10,000-eV region)"

- **C. F. Hooper, Jr.** (University of Florida): "X-Ray Framing Cameras and the Spectroscopic Analysis of Laser-Produced Implosions"
- **J. Garrett Jernigan** (University of California, Berkeley): "X-Ray Imaging of Laser-Fusion Targets Utilizing PIN Diode Arrays"
- **Chan Joshi** (University of California, Los Angeles): "Studies of Self Focusing and Filamentation Instabilities in Short-Wavelength Laser Fusion"

Further information on the National Laser Users Facility is available from:

Manager
National Laser Users Facility
Laboratory for Laser Energetics
University of Rochester
250 East River Road
Rochester, New York 14623-1299
(716) 275-2074

ACKNOWLEDGMENT

This work was supported by the U.S. Department of Energy Office of Inertial Fusion under agreement number DE-FC08-85DP40200 and the various contracts awarded users of the National Laser Users Facility

PUBLICATIONS AND CONFERENCE PRESENTATIONS

Publications

J. F. Seely, C. M. Brown, U. Feldman, M. Richardson, B. Yaakobi, and W. E. Behring, "Evidence for Gain on the C VI 182 Å Transition in a Radiation-Cooled Selenium/Formvar Plasma," *Opt. Commun.* **54**, 289–294 (1985).

Georg F. Albrecht, Mark T. Grunersen, and David Smith, "An Active Mode-Locked Q-Switched Oscillator Using Nd^{3+} Doped Glass as the Active Medium," *IEEE J. Quantum Electron.* **21**, 1189–2914 (1985).

B. L. Henke and P. A. Jaanimagi, "Two-Channel, Elliptical Analyzer Spectrograph for Absolute, Time-Resolving Time-Integrating Spectrometry of Pulsed X-Ray Sources in the 100–10,000-eV Region," *Rev. Sci. Instrum.* **56**, 1537–1552 (1985).

R. L. Schriever, J. L. Emmett, R. L. McCrory, D. Giovanielli, S. Bodner, and G. Yonas, "Progress and Directions in Inertial Fusion," *J. Fusion Energy* **4**, 115–128, (1985).

R. L. McCrory, O. Barnouin, R. S. Craxton, J. Delettrez, R. Epstein, L. Forsley, L. M. Goldman, R. J. Hutchison, R. L. Keck, H. Kim, W. Lampeter, S. A. Letzring, R. S. Marjoribanks, P. McKenty, M. C. Richardson, W. Seka, R. W. Short, A. Simon, S. Skupsky, J. M. Soures, K. Swartz, K. Tanaka, C. Verdon, and B. Yaakobi, "Short Wavelength, Direct Drive Laser Fusion Experiments at the Laboratory for Laser Energetics," in *Plasma Physics and Controlled Nuclear Fusion Research* (IAEA, Vienna, 1984), pp. 37–48.

C. J. McKinstrie and A. Simon, "Nonlinear Saturation of Stimulated Raman Scattering in a Collisional Homogeneous Plasma," *Phys. Fluids* **28**, 2602–2613 (1985).

W. Seka, B. B. Afeyan, R. Boni, L. M. Goldman, R. W. Short, and K. Tanaka, "Diagnostic Value of Odd-Integer Half-Harmonic Emission from Laser-Produced Plasmas," *Phys. Fluids* **28**, 2570–2579 (1985).

P. Bado and M. Bouvier, "Multikilohertz Pockels Cell Driver," *Rev. Sci. Instrum.* **56**, 1744–1745 (1985).

K. A. Tanaka, B. Boswell, R. S. Craxton, L. M. Goldman, F. Guglielmi, W. Seka, R. W. Short, and J. M. Soures, "Brillouin Scattering, Two-Plasmon Decay, and Self-Focusing in Underdense Ultraviolet Laser-Producing Plasma," *Phys. Fluids* **28**, 2910–2914 (1985).

R. L. McCrory, "Inertial Fusion at a Critical Juncture," Editorial, *Laser Focus*, p. 14 ff. (September 1985).

T. Sizer II, "Fast and Flexible Forth Programming in a Femtosecond Laser Lab," *Journal of Forth Applications and Research* **3**(1), 23 (1985).

Forthcoming Publications

U. Feldman, J. F. Seeley, M. C. Richardson, W. E. Behring, and S. Goldsmith, "Transitions of the Type 2s-2p in Fluorine-Like and Oxygen-Like As, Se, Br and Rb^{x}," to be published in the *Journal of the Optical Society of America B.*

P. Horn, P. Braunlich, and A. Schmid, "Photoacoustic Determination of Three-Photon Absorption Cross Sections in Thallium Halides at 1.06 μm," to be published in the *Journal of the Optical Society of America B.*

S. Williamson, G. Mourou, and J. C. M. Li, "Time-Resolved Laser-Induced Phase Transformation in Aluminum," to be published in the *Proceedings of MRS Symposium on Energy Beam-Solid Interactions and Transient Thermal Processing.*

J. F. Seeley, C. M. Brown, U. Feldman, M. Richardson, B. Yaakobi, and W. E. Behring, "Evidence for Lasing on the 182-Å Transition of CVI in a Radiation-Cooled Plasma," to be published in *Optics Communications.*

W. A. Lampeter, "Computerized Search of Chest Radiographs for Tumors," to be published in *Investigative Radiology.*

W. A. Lampeter, "ANDS-VI Computer Detection of Lung Nodules," to be published in the *Proceedings of Medical Imaging and Instrumentation 1985, Society of Photographic Scientists and Engineers.*

B. Yaakobi, R. D. Frankel, J. M. Forsyth, and J. M. Soures, "Laser Generated X-Ray Source for Time-Resolved Biological and Material Structure Studies," to be published in the *Proceedings of a Symposium on New Methods in X-Ray Absorption, Scattering, and Diffraction.*

D. P. Butler, T. Y. Hsiang, and G. A. Mourou, "Transient Relaxation of the Normal State Resistance of Tin Microstrips in the Presence of Current Bias," to be published in the *Journal of Low Temperature Physics.*

The following papers are to be published in the *Proceedings of the Workshop on Physics of Laser Fusion*, Vancouver, B.C., June 1985 (*Canadian Journal of Physics*):

A. Simon, "Raman Scattering."

J. Delettrez, "Thermal Electron Transport in Direct-Drive ICF."

L. M. Goldman, "The Use of Laser Harmonic Spectroscopy as a Target Diagnostic."

M. D. J. Burgess, R. Dragila, B. Luther-Davies, K. A. Nugent, A. J. Perry, G. J. Tallents, M. C. Richardson, and R. S. Craxton, "Characterization of Plasmas Produced by a Laser Line Focus," to be published in *Physical Review A.*

W. R. Donaldson and G. A Mourou, "Improved Contacts on Intrinsic Silicon for High Voltage Photoconductive Switching," to be published in the *Proceedings of the Fifth IEEE Pulsed Power Conference*, Arlington, VA, June 1985.

The following papers are to be published in the *Proceedings of the SPIE 29th Annual International Technical Symposium on Optical and Electro-Optic Engineering,* San Diego, CA, August 1985:

G. G. Gregory, S. A. Letzring, M. C. Richardson, and C. D. Kiikka, "High Time-Space Resolved Photography of Laser Imploded Fusion Targets."

P. A. Jaanimagi, B. L. Henke, and M. C. Richardson, "An Absolutely Calibrated Time-Resolving X-Ray Spectrometer."

M. C. Richardson, G. G. Gregory, S. A. Letzring, R. S. Marjoribanks, B. Yaakobi, B. L. Henke, P. A. Jaanimagi, and A. Hauer, "Time-Resolved X-Ray Spectrographic Instrumentation for Laser Fusion and X-Ray Laser Studies."

R. L. McCrory, "Inertial Confinement Fusion (ICF)," to be published in *Physics Today*, January 1986.

D. Strickland and G. Mourou, "Compression of Amplified Chirped Optical Pulses," to be published in *Optics Communications*.

R. Epstein, S. Skupsky, and J. Delettrez, "Effects of Non-Maxwellian Electron Populations in Non-LTE Simulations of Laser-Plasma Thermal and Implosion Experiments," to be published in the *Journal of Quantitative Spectroscopy and Radiative Transfer.*

A. Simon, W. Seka, L. M. Goldman, and R. W. Short, "Raman Scattering in Inhomogeneous Laser Produced Plasma," to be published in *Physics of Fluids.*

R. S. Craxton, R. L. McCrory, and J. M. Soures, "Progress Towards Controlled Thermonuclear Fusion Using Frequency-Converted Lasers," to be published in *Scientific American.*

M. C. Richardson, R. Epstein, O. Barnouin, P. A. Jaanimagi, R. Keck, H. G. Kim, R. S. Marjoribanks, S. Noyes, J. M. Soures, and B. Yaakobi, "Multibeam, Laser-Imploded Cylindrical Plasmas," to be published in *Physical Review A.*

A. Hauer, R. D. Cowan, B. Yaakobi, O. Barnouin, and R. Epstein, "Absorption Spectroscopy Diagnosis of Pusher Conditions," to be published in *Physical Review*.

R. Epstein and R. S. Craxton, "Stastical Ray Tracing in Plasmas with Random Density Fluctuations," to be published in *Physical Review*.

B. Yaakobi, "X-Ray Diagnostic Methods for Laser Imploded Targets" and "Thermal Transport, Mass-Ablation, and Preheat in Laser-Target Experiments," to be published in the *Proceedings of the Spring College on Radiation in Plasmas*, Trieste, Italy, June 1985 (World Scientific Publishing Co.).

The following papers are to be published in *Picosecond Electronics and Optoelectronics*, edited by G. A. Mourou, D. Bloom, and C. H. Lee (Springer-Verlag, Berlin, Heidelberg, New York, Tokyo, 1985):

K. E. Meyer and G. A. Mourou, "Two Dimensional E-Field Mapping with Subpicosecond Resolution."

S. Williamson and G. A. Mourou, "Picosecond Electro-Electron Optic Oscilloscope."

K. E. Meyer, D. R. Dykaar, and G. A. Mourou, "Characterization of TEGFETs and MESFETs Using Electro-Optic Sampling Technique."

C. J. Kryzak, K. E. Meyer, and G. A. Mourou, "Transmission Line Designs with a Measured Step Response of 3 ps per Centimeter."

D. R. Dykaar, T. Y. Hsiang, and G. A. Mourou, "Development of a Picosecond Cryo-Sampler Using Electro-Optic Techniques."

Conference Presentations

The following presentations were made at the SPIE 29th Annual International Technical Symposium on Optical and Electro-Optic Engineering, San Diego, CA, August 1985:

G. G. Gregory, S. A. Letzring, M. C. Richardson, and C. D. Kiikka, "High Time-Space Resolved Photography of Laser Imploded Fusion Targets."

P. A. Jaanimagi, B. L. Henke, and M. C. Richardson, "An Absolutely Calibrated Time-Resolving X-Ray Spectrometer."

M. C. Richardson, G. Gregory, S. A. Letzring, R. S. Marjoribanks, B. Yaakobi, B. L. Henke, P. A. Jaanimagi, and A. Hauer, "Time-Resolved X-Ray Spectrographic Instrumentation for Laser Fusion and X-Ray Laser Studies."

W. Donaldson and G. Mourou, "Problems of High Power Photoconductive Switching in the Picosecond Time Scale," presented at New Directions in Solid State Power Switching, Farmingdale, NY, August 1985.

A. Simon, "Theory of Raman Scattering in Laser-Produced Plasma," presented at the CECAM Workshop on Interactions and Transport in Laser Plasmas, Orsay, Paris, September 1985.

The work described in this volume includes current research at the Laboratory for Laser Energetics which is supported by Empire State Electric Energy Research Corporation, General Electric Company, New York State Energy Research and Development Authority, Northeast Utilities Service Company, Ontario Hydro, Southern California Edison Company, The Standard Oil Company, University of Rochester, and the U.S. Department of Energy Office of Inertial Fusion under agreement DE-FC08-85DP40200.